



Layered by layered Ni-Mn-LDH/g-C₃N₄ nanohybrid for multi-purpose photo/electrocatalysis: Morphology controlled strategy for effective charge carriers separation

Muhammad Shakeel, Muhammad Arif, Ghulam Yasin, Baoshan Li*, Hashmat Daud Khan

State Key Laboratory of Chemical Resource Engineering, Beijing University of Chemical Technology, Beijing, 100029, PR China

ARTICLE INFO

Keywords:

Layered by layered nanohybrid
Band gap adjustment
Efficient charge transportation
Visible light induced photo/electrocatalytic activity
OER
HER
Degradation of RhB

ABSTRACT

The earth copious extremely active photo/electrocatalysts have been of immense interest for hydrogen evolution reaction (HER), oxygen evolution reaction (OER) together with environment purification. However, the efficiency of photo/electrocatalysis is still low because of the less visible light absorption and fast recombination of electron-hole pairs. Herein taking the benefits of layered and electronic structural design of Ni-Mn-layered double hydroxide and layered graphitic carbon nitride. A novel Ni-Mn-LDH/g-C₃N₄ heterostructured photo/electrocatalyst with suited bands was in situ constructed by temperature controlled hydrothermal treatment. A turn in band gap energy within the range of Ni-Mn-LDH to g-C₃N₄ was noted through a series of physicochemical techniques. Consequently the optimized nanohybrid Ni-Mn-LDH/g-C₃N₄ (10%) used as best electrocatalyst with $J_{OER} = 10 \text{ mAcm}^{-2}$ @ 316 mV and $J_{HER} = -60 \text{ mAcm}^{-2}$ @ -147 mV). Furthermore under visible light illumination it function as outperformed photo/electrocatalyst with $J_{OER} = 10 \text{ mAcm}^{-2}$ @ 296 mV and $J_{HER} = -60 \text{ mAcm}^{-2}$ @ -126 mV in 1 M KOH with a super stability. Similarly it was used for the degradation of RhB with outperformance ($\geq 99\%$) and rate constant $k = 0.313 \text{ min}^{-1}$. Rivaling the performance of expensive catalysts such as RuO₂ and Pt/C and other counterparts. The enhanced photo/electrocatalytic activity ascribed to the formation of band-matched layered by layered heterojunction-accelerated charge separation. It is predicted that our temperature controlled strategy based on earth-profuse elements with structural reliability providing an innovative and inexpensive photo/electrocatalytic system for realistic energy conversion applications.

1. Introduction

Electrochemistry has been intensely researched in the pursue of sustainable and efficient energy conversion by photo/electrocatalytic water splitting together with purification of environment by the photocatalytic degradation of dyes [1,2]. A lot of efforts have been made to dealing with the issues in the last decades by using advance photo/electrocatalysts [3–5]. But there are still foremost problems needing to address such as high absorption of visible light, suitable band positions for efficient charge transportation and high stability are extremely desirable for effective photo/electrocatalysis [5]. The electronic structure, crystal structure and surface morphology tremendously effect the performance of photo/electrocatalyst [6]. However by selecting the appropriate material with proper fitting of band edges corresponding to electronic structure, the effective photo/electrocatalytic system for OER, HER water splitting and for photocatalytic degradation of dyes can be structured. Numerous strategies successfully widened the

absorption band of UV-active materials by doping with cations [7–9], with anions [5,10] and by decorating with plasmonic materials [11,12]. 3d LDH of Ni, Co, Mn, Cu, Zn and Fe were considered as a vital class of layered materials, taking an immense attention due to their diverse applications in photocatalysis, electrochemistry, biomedical science, magnetization, polymerization and in environmental science [13,14]. The pure and modified LDHs have been reported for photocatalytic degradation and splitting of water into hydrogen and oxygen, owing to their exceptional layered structure, compositional flexibility, low manufacturing cost and ease to synthesis [15]. Beside current advancement, the fabrication of visible light active LDH based photo/electrocatalytic system is a subject of fastidious significance [16–23]. The nontoxic and abundant materials (g-C₃N₄) have also broadly investigated for photocatalytic environmental purification and photo/electrocatalytic water splitting [24–26]. Accordingly, the coupling of LDHs with layered polymeric graphitic-carbon nitride (g-C₃N₄) have boost up the desired photo/electrocatalytic performance under

* Corresponding author.

E-mail address: bsli@mail.buct.edu.cn (B. Li).

<https://doi.org/10.1016/j.apcatb.2018.10.005>

Received 31 July 2018; Received in revised form 25 September 2018; Accepted 5 October 2018

Available online 08 October 2018

0926-3373/ © 2018 Elsevier B.V. All rights reserved.

visible light radiations [27,28]. Owing towards structural and electronic properties, g-C₃N₄ has all the fundamentals for heterogeneous photo/electrocatalysis. This group has good conductivity and an appropriate band gap prevail the endothermic character of the photo/electrocatalytic water-splitting together with the photocatalytic degradation of organic dyes [15,29–32]. A heterojunction facilitates the charge carriers transportation due to optimum band positions of two semiconductors. By absorbing visible light electrons are excited from the VB into the CB and shifting of electrons and holes at the interfaces of the hetero-junction used to perform photo/electrocatalytic reactions [33]. The complex designing of functional groups in such type of heterostructure is an obstacle for the required applications [4,34–36]. Recently morphology controlled fabrications have taken more consideration because of its excellent photo/electrocatalytic efficiency. Previously we reported the visible light responsive mesoporous nanocomposite and LDH based materials with remarkable photo/electrocatalytic behavior for environmental remediation and oxidation of water [37,38].

The aim of present investigation basically a motivation to design layered by layered nanohybrid having suitable electronic structure by synergistic coupling of Ni-Mn-LDH and layered graphitic carbon nitride via. in-situ hydrothermal treatment at controlled temperature (180 °C). The high layered charge density along 2-D interlayer spaces of flexible height create a streamlined path way for the visible light absorption and electron transportation due to matched band potentials and displayed excellent photo/electrocatalytic behavior in OER, HER water splitting and photocatalytic dyes degradation. This investigation provided an up-to-date progress to control the energy crises and environmental pollution remediation.

2. Experimental section

2.1. Material

Ni(NO₃)₂·6H₂O, MnCl₂·4H₂O, CH₃OH and dicyandiamide (DCDA) was purchased from Beijing Chemicals Reagent Co., Ltd. China.

2.2. Fabrication of g-C₃N₄ nanosheets

The bulk g-C₃N₄ was synthesized by the thermal treatment of DCDA. In a typical experiment definite amount of DCDA was calcined in muffle furnace at 550 °C for 4h@3 °Cmin⁻¹ [39]. The deep yellow powder was grinded till it became light yellow powder of the bulk g-C₃N₄ followed by further heating at 600 °C for 2h@5 °Cmin⁻¹ to be converted into g-C₃N₄ nano sheets.

2.3. Fabrication of the layered by layered Ni-Mn-LDH/g-C₃N₄ nanohybrids

The Ni-Mn-LDH/g-C₃N₄ nanohybrids were prepared by in-situ hydrothermal process (see Scheme 2). A definite quantity of the thermodynamically stable g-C₃N₄ nanosheets were dropped into a mixture of H₂O/CH₃OH (1:3) and ultrasonically treated for 45 min. The Ni(NO₃)₂·6H₂O and MnCl₂·4H₂O (0.8 mmol) as Ni and Mn precursors was then dropped into homogeneous dispersion of g-C₃N₄ nano sheets and was further sonicated for 60 min. This allowed the metal cations to adsorb on g-C₃N₄ via electrostatic interactions. Afterward, the suspension was divided into four fractions and hydrothermally treated at 100 °C, 150 °C, 180 °C and 200 °C for 12 h to get the optimized sample. No stabilizing agent and control sample was needed in this reaction due to high thermodynamic stability (up to 600 °C) of g-C₃N₄ [31,40,41]. After autoclaving the precipitates were washed with C₂H₅OH and deionized H₂O and finally with acetone yielding Ni-Mn-LDH/g-C₃N₄(x %) nanohybrids. x stand for g-C₃N₄ nano sheets. The resulting nanohybrids designated as Ni-Mn-LDH/g-C₃N₄ (5%), Ni-Mn-LDH/g-C₃N₄ (10%) and Ni-Mn-LDH/g-C₃N₄ (15%). Ni-Mn-LDH was also synthesized by following the same procedure without g-C₃N₄ nano sheets.

2.4. Fabrication of the Ni(OH)₂/g-C₃N₄ and Mn(OH)₂/g-C₃N₄ powder

For comparative studies powder of Ni(OH)₂/g-C₃N₄ and Mn(OH)₂/g-C₃N₄ were also prepared with 10% mass loading of g-C₃N₄ by using the same procedure. In usual synthesis, definite quantity of g-C₃N₄ nano sheets was ultrasonically dispersed in a mixture of 15 ml of H₂O and 65 ml of CH₃OH. Then calculated amount of each Ni(NO₃)₂·6H₂O and MnCl₂·4H₂O was then dropped into the above homogeneous dispersion and was further sonicated for 60 min. Afterward the suspension was hydrothermally treated at 180 °C for 12 h. The precipitates were collected and washed to yield the Ni(OH)₂/g-C₃N₄ and Mn(OH)₂/g-C₃N₄.

2.5. Characterization of the as prepared materials

The crystalline structure was characterized by XRD on a Rigaku D/Max 2500 VBZ+/PC diffraction meter using Cu-Kα radiations (λ = 0.1541 nm). The scanning for crystalline diffractions was carried out at 2θ range of 10–70°. Surface properties and micro structure was analyzed by SEM (Hitachi S-4700) and HRTEM (JEM-3010) with SEM elemental spectral graph and elemental mapping. The UV-vis./DR spectra were taken using UV-vis./NIR spectrophotometer UV-3600 (Shimadzu) cary 500 scan with an integrating sphere attachment. BaSO₄ was used for the calibration of the standard line before measuring the absorbance.

The photoluminescence (PL) spectra were taken using Hitachi analytical instrument Model F-7000, Fluorescence Spectrophotometer with an excitation wavelength of 320 nm and 470 nm.

The valance state and binding energies were investigated by XPS on ESCALAB-250 X-ray photoelectron spectrometer having monochromated light (Al-Kα X-ray). The survey energy is 200 eV and for high resolution scan is 30 eV. The C 1s peak at 284.6 eV was used for the calibration of binding energy. Spin trapping experiments were carried out on analytical instrument Bruker model E-500 spectrometer to identify the Reactive oxygen species (ROSs) taking a part in photocatalytic reactions. The Nitrogen adsorption and desorption isotherm was measured for surface area on specific surface area analyzer (Micromeritics ASAP2020M instrument). The powder material was degassed in vacuum at 573 K for 6 h before measurements and surface area was calculated by using Brunauer-Emmett-Teller (BET) equation. The chemical compositions of the nanohybrids were measured by Inductive Coupled Plasma by ICP-MS and Elemental Analyzer system GmbH (Vario EL cube superuser).

2.6. Electrochemical measurements

The OER and HER electrochemical performance of nanohybrids were investigated in 1M KOH solution. Measurements were carried out on three-electrode electrochemical cell (CHI 760E CH Instrument Co. USA) assembled with Pt wire as counter, Ag/AgCl (PINE, 4M KCl) as reference and the GC electrode (3 mm) used as working electrode respectively. Usually 5 mg of the catalyst sonicated in a mixture of 1 mL conductivity water, 250 μL of isopropyl alcohol and 10 μL of Nafion solution acquired homogeneous ink. Subsequently 10 μL of this was loaded onto the GC electrode and was allowed to dry. The measurement system was calibrated and the corresponding OER and HER polarization curves were recorded after iR-corrections. During the measurements working electrode was continuously rotating at 1600 rpm to remove the generated oxygen and hydrogen bubbles.

2.7. Photo electrochemical measurements (PEC)

The photo electrochemical measurements (PEC) were carried out on (CHI 760C electrochemical workstation) with three-electrode system, consist of Pt wire as counter electrode, GC as working electrode and Ag/AgCl system as reference electrodes. The reactions were performed in 1M KOH as an electrolyte. During the reaction the working electrode

was illuminated using 300 W xenon lamp with an AM 1.5G filter (Newport 81094) having illumination intensity of 100 mWcm^{-2} . The light was passed through a UV filter (UV to the visible region at $\lambda \approx 450 \text{ nm}$) then focused on the working electrode.

2.8. Photocatalytic degradation of dyes

The photocatalytic degradation activity of the Ni-Mn-LDH/g-C₃N₄ nanohybrids and other reference samples were measured under visible light. Typically 0.1 g of the catalyst was dispersed in 100 mL of RhB (50 mg L^{-1}). First ensure an adsorption-desorption equilibrium in dark then exposed to Hg lamp with a cutoff filter as the visible light source ($\lambda > 420 \text{ nm}$) with constant stirring [42]. The lamp was positioned at 10 cm away from the reaction cell to activate the photocatalytic reactions. At each interval, the appropriate amount of suspension was pipette out, the powder was removed and photocatalytic degradation of RhB was measured by colorimetric method. No degradation was found in the absence of the catalyst and/or the irradiations. The change in concentration before and after degradation was measured by comparing the absorption peak with the standard calibration curve.

3. Results and discussion

3.1. Structure characterizations

The characteristics crystallographic structure of Ni-Mn-LDH, g-C₃N₄ nano sheets, and Ni-Mn-LDH/g-C₃N₄ nanohybrids with diverse amount of g-C₃N₄ are shown in Fig. 1. The g-C₃N₄ nano sheets usually exhibited very feeble peak at 13.1° (100) and more distinct peak at 27.5° indexed to (002) planes of hexagonal graphitic carbon structure, ascribe to the inter-layer packing and inter planar stacking peaks of the aromatic system respectively [43,44]. Whereas the peaks at 11.4° , 23.1° , 34.1° , 38.6° , 46.1° , 59.5° and 60.9° indexed as (003), (006), (012), (015), (018), (110), and (113) respectively and were the distinctive diffractions of the hydrotalcitic crystalline structure of Ni-Mn-LDH/g-C₃N₄ nanohybrids [45]. The peak intensity at 27.5° raised without disturbing the peaks position of Ni-Mn-LDH by escalating the mass of g-C₃N₄ nano sheets on LDH. It meant that the crystal growth of g-C₃N₄ nano sheets did not obstruct the crystal growth of Ni-Mn-LDH. Hence it could be inferred that the crystalline structure of g-C₃N₄ and Ni-Mn-LDH remained unchanged after modification leading to the formation of the exotic Ni-Mn-LDH/g-C₃N₄ nanohybrid that is more beneficial for

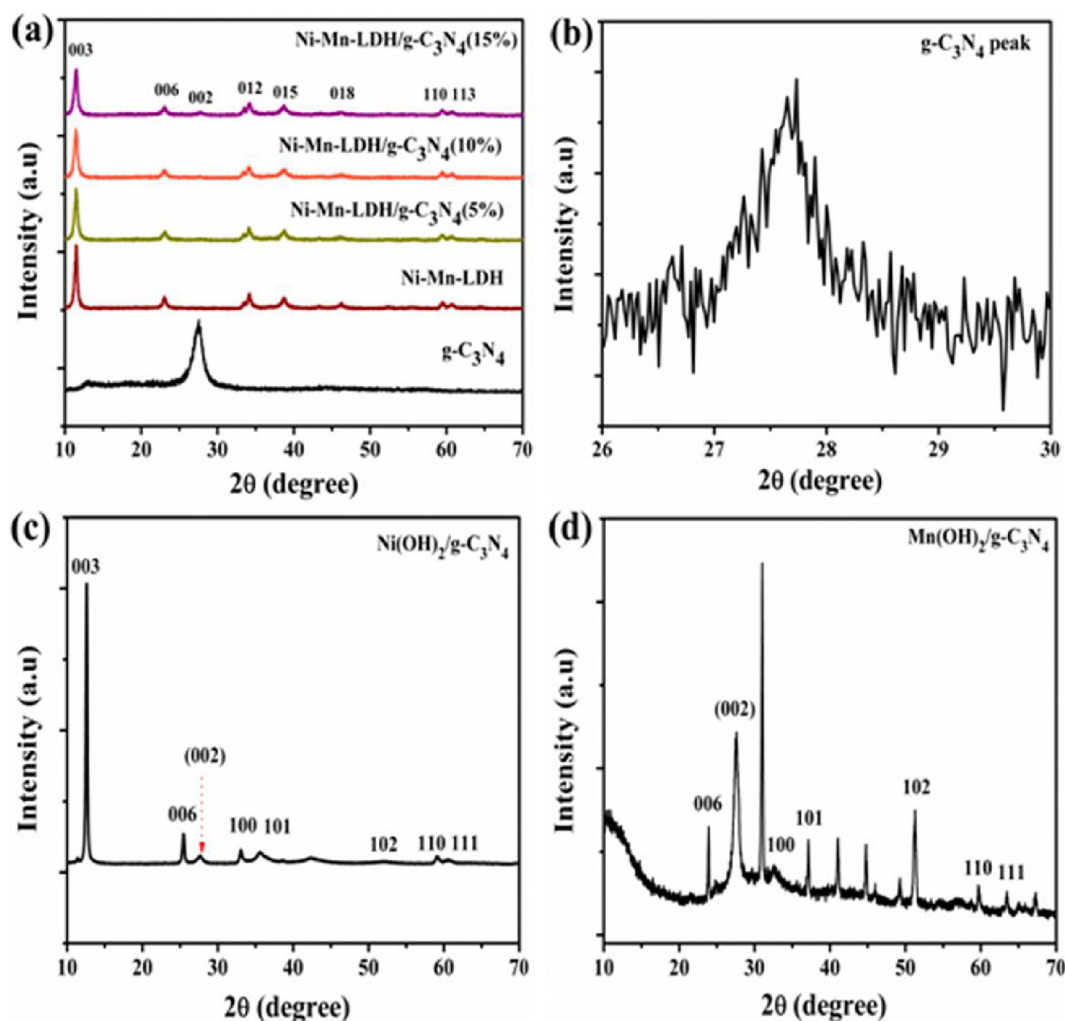


Fig. 1. (a) The XRD of g-C₃N₄, Ni-Mn-LDH and Ni-Mn-LDH/g-C₃N₄ nanohybrids with different mass loading of g-C₃N₄ (b) Partial enlarge view of the peak of g-C₃N₄ at 27.5° (002) of Ni-Mn-LDH/g-C₃N₄ (10%) nanohybrid. XRD of (c) Ni (OH)₂/g-C₃N₄ (d) Mn (OH)₂/g-C₃N₄.

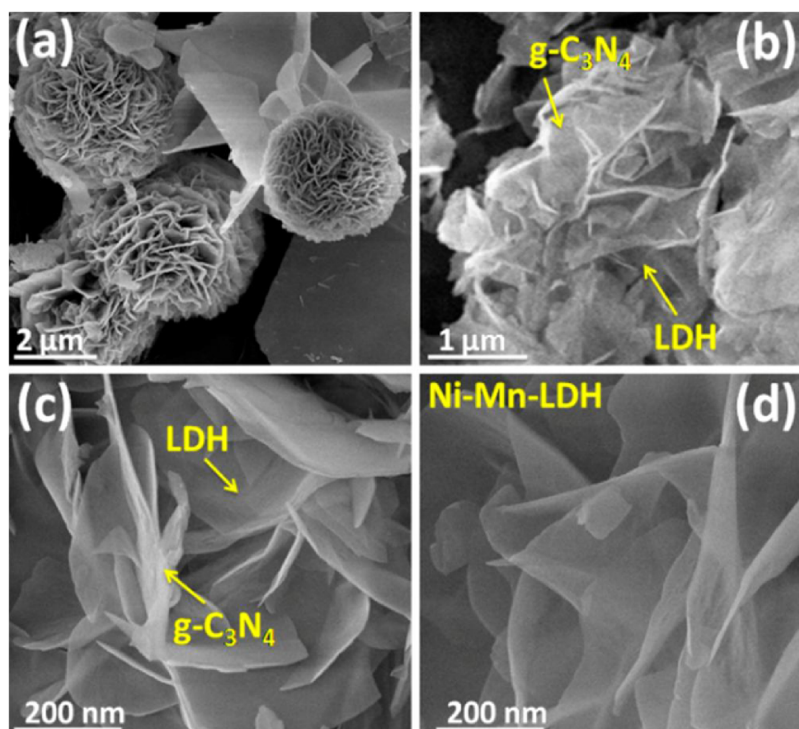


Fig. 2. (a–c) SEM images of Ni-Mn-LDH/g-C₃N₄ (10%) nanohybrid (d) Ni-Mn-LDH.

photo/electrocatalytic applications [46,47]. In order to highlight the superiority of LDH structure, the XRD spectra of Ni(OH)₂/g-C₃N₄ and Mn(OH)₂/g-C₃N₄ were also taken for comparison. It could be seen that the peaks indexed as (003), (006), (002), (100), (101), (102), (110) and (111) corresponding to various crystal planes of Ni(OH)₂/g-C₃N₄ and Mn(OH)₂/g-C₃N₄. Whereas (012), (015), (018) crystal planes are missing in Ni(OH)₂/g-C₃N₄ and Mn(OH)₂/g-C₃N₄ compare to Ni-Mn-LDH/g-C₃N₄ nanohybrid which is the distinctive property of LDH [48–50]. In addition the extra peaks appeared at 30.9°, 41.2° and 44.8° in Mn(OH)₂/g-C₃N₄ ascribed to crystalline structure of Mn₃O₄ [51]. Of note, the positive shifting of diffraction angles on (003) and (006) planes of Ni(OH)₂/g-C₃N₄ and Mn(OH)₂/g-C₃N₄ due to diminish d spacing along the c-axis most probably due to the intercalation of the g-C₃N₄ in the Ni(OH)₂ and Mn(OH)₂ lattice [52,53].

The surface morphology and micro-structure were analyzed by SEM and HRTEM. The SEM consequences of Ni-Mn-LDH/g-C₃N₄ nanohybrids possesses regularly distributed shrivel and curly interconnected 2D nano sheets with thickness about several tens of nanometer and 200–500 nm lateral dimensions. These are stacked over one another to form layered by layered structure, comprising g-C₃N₄ layered material that entirely covered the whole surface of layered Ni-Mn-LDH in the form of thin cloudy nano sheets are shown in Fig. 2a–c. These characteristics demonstrated the well-built interactions between two layered materials either through charge transfer interactions or electrostatic interactions, which is very appropriate for visible light absorption and charge transportation [54–56]. This is divergent to pure Ni-Mn-LDH having spanning and wide gape nanosheets, and less connectivity with the neighboring nano sheets are shown in Fig. 2d. It is also observed from SEM images of Ni-Mn-LDH/g-C₃N₄ nanohybrids that the Ni-Mn-LDH and g-C₃N₄ nano sheets are uniformly enclosed by intercrossing each other originating copious voids. These voids increase the specific surface area to 360 m² g^{−1} (IV-typed N₂ adsorption/desorption isotherm) (Figure S₉). Such type of open and flexible structure will assist to induce more reaction sites, shorten the ions transport distance and make sure the adequate photo/electrocatalytic reactions [57]. The SEM images of Ni-Mn-LDH/g-C₃N₄ nano hybrids synthesized

at 100 °C, 150 °C and 200 °C have been provided in supplementary Figure S₈. It can be noted that the hydrothermal treatment below and above the optimal temperature leads to the structural stacking of LDHs nano sheets to build aggregates. This agglomeration is very stable and resistant to de-cohesion even under powerful ultrasonic treatment.

Hence the thickness of the nano sheets increases while the interaction force between the layered materials could be weakening that hinder the transportation of photo generated charge carriers.

Furthermore the micro structure of Ni-Mn-LDH and Ni-Mn-LDH/g-C₃N₄ nanohybrids with related SAED pattern investigated by HRTEM analysis. Figures S_{3–5} gives information about the microstructure, reveals the distinctive interfaces between Ni-Mn-LDH and g-C₃N₄ nano sheets. The inter planar distance of 0.26 and 0.23 nm, indexed as (012) and (015) are the characteristics crystallographic plane of Ni-Mn-LDH also found in Ni-Mn-LDH/g-C₃N₄ nanohybrids. While the 0.321 nm (002) ascribed to graphitic g-C₃N₄ are shown in Fig. 3. From the SAED pattern of Ni-Mn-LDH/g-C₃N₄ several concentric rings were observed that demonstrating the constant overlapping of g-C₃N₄ nano sheets on Ni-Mn-LDH. It verified the insignificant effect of g-C₃N₄ nano sheets on the crystal structure of Ni-Mn-LDH consistent with the XRD results. It could assist to increase the ECSA and are more beneficial for visible light absorption and transportation of photo generated charge carriers between Ni-Mn LDH and g-C₃N₄ with prolong recombination [58,59].

The elemental analysis of Ni-Mn-LDH/g-C₃N₄ nanohybrid evidently demonstrated the configuration of Ni, Mn, C, N and O elements within the nanohybrid. The EDS spectral graph and the corresponding elemental mapping of Ni-Mn-LDH/g-C₃N₄ are displayed in Fig. 4. In addition the chemical compositions of the as prepared nanohybrids were measured by inductive coupled plasma analysis and by elemental analysis system. The corresponding results have the same mass contents as used in the initial precursors (Table 1 SI).

The surface chemical composition and valance states of the elements were investigated by XPS. The survey spectra depicted the existence of C, O, N, Ni, and Mn in Ni-Mn-LDH/g-C₃N₄ nanohybrids (Fig. 5a). The deconvolution peak fitting of C 1s spectrum corresponding to O and N functional groups. This is included (O–C=O, 288.6 eV),

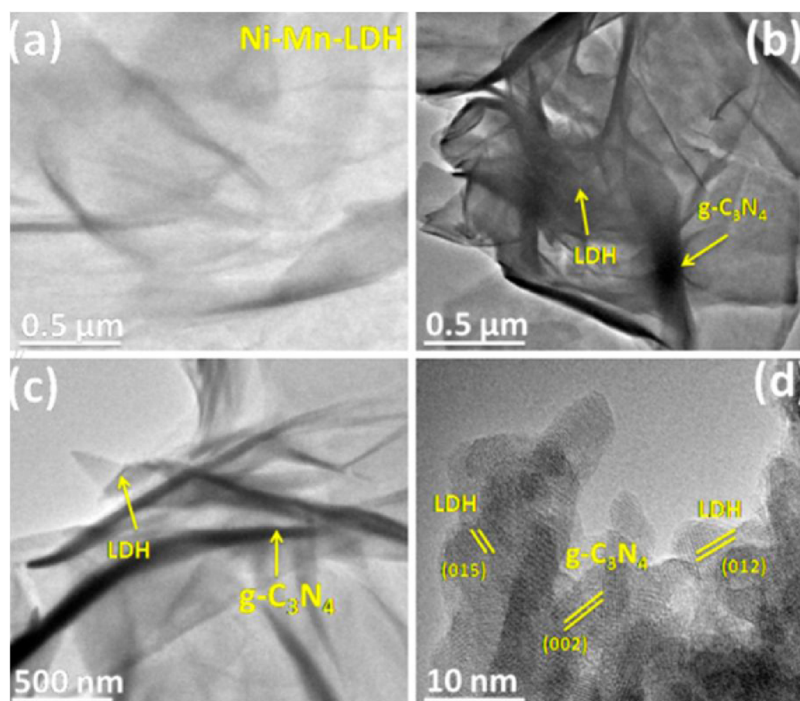


Fig. 3. HRTEM images of (a) Ni-Mn-LDH (b–d) Ni-Mn-LDH/g-C₃N₄ (10%) nanohybrid.

(C=O, 286.5 eV), sp³ carbons (C–O, 285.5 eV), sp² carbons (C=C, 284.4 eV) and (N–C=N, 288.2 eV) [45,47] (Fig. 5b). These O and N functional groups will act as nucleation centers of LDH that built in-situ contact with g-C₃N₄ [58]. The Ni 2p and Mn 2p spectra of Ni-Mn-LDH/g-C₃N₄ nanohybrid split into 2p_{1/2} and 2p_{3/2} due to spin-orbit coupling. The Ni 2p_{3/2} peak was fitted with the characteristics of Ni²⁺ (2p_{3/2} peak at 856.1 eV) and Ni³⁺ (2p_{3/2} peak at 854.5 eV), surely corroborate the existence of Ni(OH)₂ in Ni-Mn-LDH/g-C₃N₄ [60] (Fig. 5c). Similarly the deconvolution peak fitting of Mn 2p_{3/2} further confirm the characteristic peak of Mn³⁺ (2p_{3/2} peak at 642.0 eV) and Mn⁴⁺ (2p_{3/2} peak at 644.6 eV) [51,61] (Fig. 5d). It is demonstrated that a part of Ni and Mn atoms in Ni-Mn-LDH/g-C₃N₄ exist in high valence states (Ni^{2+/3+} and Mn^{3+/4+}) and considered as active centers for photo/electrocatalytic properties [62].

The UV–vis/DR spectra of Ni-Mn-LDH, g-C₃N₄ and Ni-Mn-LDH/g-C₃N₄ nanohybrids are displayed in Fig. 6a. The Ni-Mn-LDH showed absorption bands under 200–400 nm and 600–800 nm attributed to charge transfer from O_{2p} to 3d orbital of Ni and Mn (O_{2p}/Ni_{3d-t2g}, O_{2p}/Mn_{3d-t2g}) [63,64]. The g-C₃N₄ showed an intrinsic semiconductor like absorption spectra with band edge of 450 nm and assign to n-π* direct transition of lone pairs on N atoms.

Literally, the modification of Ni-Mn-LDH with g-C₃N₄ broadly alters the optical properties in the resultant Ni-Mn-LDH/g-C₃N₄ nanohybrids. It was observed that all the modified nanohybrids exhibited a considerable absorption in the whole visible light spectrum. By successive loading of g-C₃N₄, an optimal change of the absorption edges were observed due to the strong interactions between g-C₃N₄ and Ni-Mn-LDH in nanohybrids [65]. The strong visible light absorption ability of Ni-Mn-LDH/g-C₃N₄ nanohybrids is due to dual role played by delocalized conjugated structure of g-C₃N₄ (1 s/π* and 1 s/σ*) transitions and Ni-Mn-LDH (LMCT and d-d) transitions [46,66]. The maximum absorption was found in Ni-Mn-LDH having 10% g-C₃N₄, while the minimum absorption was noted in Ni-Mn-LDH having 15% g-C₃N₄. This is due to the surface saturation with g-C₃N₄ nano sheets, that disturb the layered structure and block the active sites on the surface of Ni-Mn-LDH which unable to do electronic excitation under irradiations [46]. It could be ascribed to the well-built interfaces of g-C₃N₄ and Ni-Mn-LDH that effect the energy region [42,67].

The band gap energy (E_g) of the crystalline semiconductors can be calculated by following Eq. [68]. $(ah\nu)^{1/n} = A(h\nu - E_g)$

Where a , h , ν , E_g and A are the various fundamental constants. The, n was calculated by the type of semiconductor optical transitions, its value is $n = 1/2$ for direct transition [23]. Therefore, the plot of $(ah\nu)^2$ vs $h\nu$ (Kubelka-Munk function as a function of light energy) gives the value of $E_g = 2.18, 2.15, 2.02, 2.55$ and 2.70 eV corresponding to Ni-Mn-LDH, Ni-Mn-LDH/g-C₃N₄ (5%), Ni-Mn-LDH/g-C₃N₄ (10%), Ni-Mn-

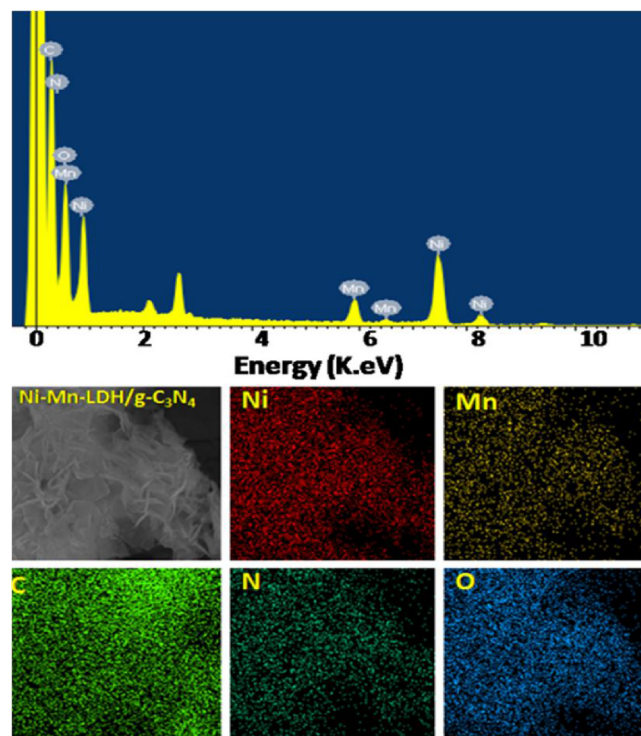


Fig. 4. EDS elemental analysis and the corresponding mapping of Ni-Mn-LDH/g-C₃N₄ (10%) nanohybrid.

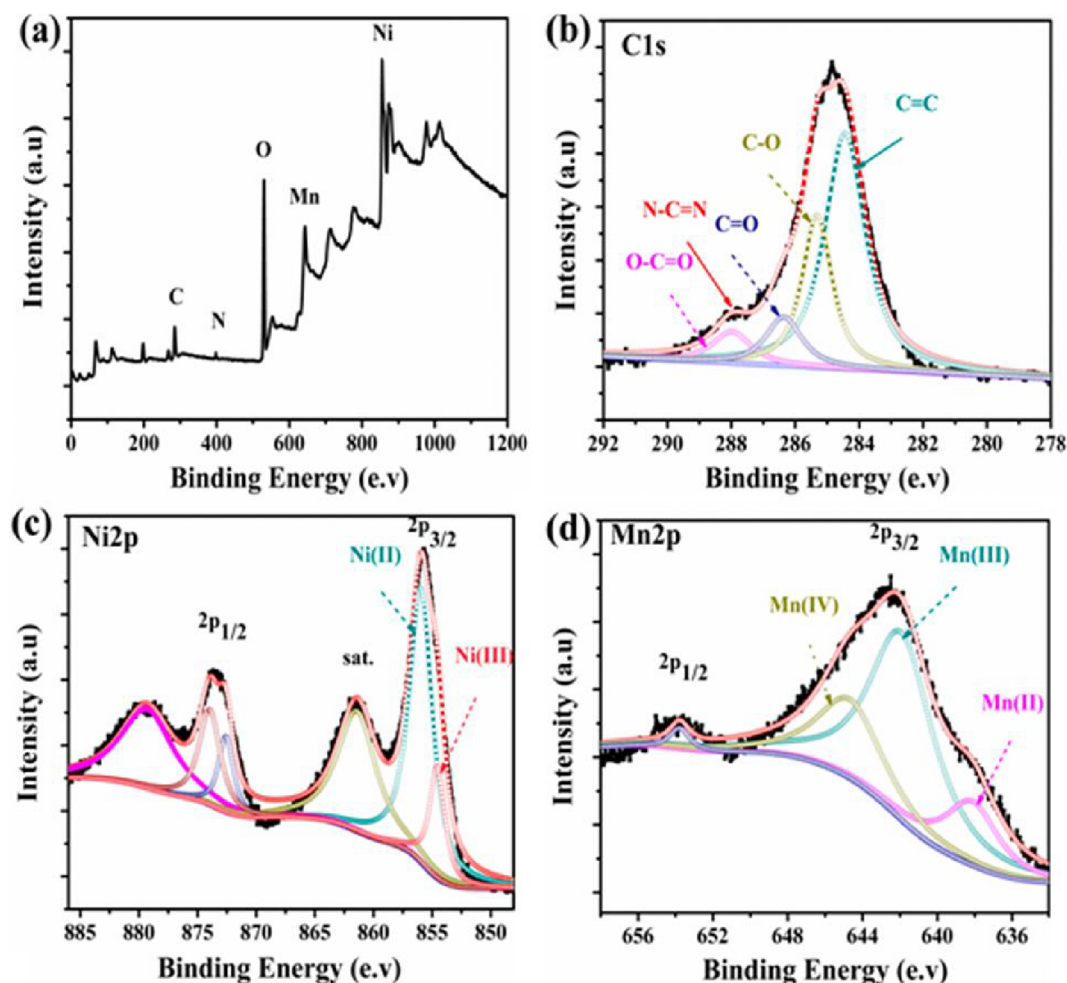


Fig. 5. (a) Full scan XPS survey spectra of Ni-Mn-LDH and Ni-Mn-LDH/g-C₃N₄ nanohybrid (b) High resolution spectrum C 1 s (c) Ni 2p (d) Mn 2p of Ni-Mn-LDH/g-C₃N₄ (10%) nanohybrid.

LDH/g-C₃N₄ (15%) and g-C₃N₄ nanosheets respectively are shown in Fig. 6b. The band gap investigations confirmed the visible-light responses of Ni-Mn-LDH/g-C₃N₄ nanohybrids due to systematic layered by layered structure and to do possible electronic transitions [15].

The separation and recombination rate of the photo generated electron-hole pairs were investigated by photoluminescence spectroscopy; corresponding results are displayed in Fig. 7a. Herein, the PL spectra were used to analyze the charge transfer behavior between Ni-Mn-LDH and g-C₃N₄. The broad peak centered at 440 to 450 nm, associated with the typical photoemission of g-C₃N₄ close to its band gap energy (2.7 eV). Similarly it is manifested that the broad band and high intensity peak of Ni-Mn-LDH assigned to the fast recombination of charges [57]. While the Ni-Mn-LDH/g-C₃N₄ nanohybrids exhibited significantly quenched and inferior intensity emission spectrum due to the synergistic coupling of Ni-Mn-LDH and g-C₃N₄ nano sheets. The maximum quenching was found in Ni-Mn-LDH/g-C₃N₄ (10%) nanohybrid associated to the dynamic and fast transportation of charge carriers with suppressed recombination [58,69]. While minimum quenching and broad peak was observed in Ni-Mn-LDH/g-C₃N₄ (15%) nanohybrid. This is due to excess of g-C₃N₄ leading to the shielding effect and block the active sites on the catalyst surface [70]. These facts also verified the suitable electronic coupling of g-C₃N₄ and Ni-Mn-LDH that enhances the transportation of the photo generated charges throughout the layered structure via energy transfer. Moreover the PL spectra of the

photo/electrocatalysts were also taken using excitation wavelength higher than the band gap of g-C₃N₄ to investigate the effect of Ni-Mn-LDH/g-C₃N₄ heterojunction as well to show the contribution of g-C₃N₄ on charge separation of Ni-Mn-LDH. It could be seen from the Fig. 7b that the Ni-Mn-LDH/g-C₃N₄ nanohybrids with different g-C₃N₄ content exhibited the PL spectrum almost at the same position with weak peak intensity, indicating the negligible contribution of g-C₃N₄ at higher excitation wave length because of insufficient supplied energy than required for electronic excitation between VB and CB. A semiconductor cannot absorb the photons having energy less than the band gap. Hence this phenomenon explains the tremendous contribution of g-C₃N₄ in Ni-Mn-LDH/g-C₃N₄ heterojunction on charge separation of Ni-Mn-LDH.

4. Photo/electrochemical properties

We investigated the OER and HER photo/electrochemical performance of the as prepared photo/electrocatalysts in alkaline solution (1 M KOH) in a standard three-electrode system. The catalyst was evenly casted onto a glassy carbon (GC) electrode (loading $\approx 10 \mu\text{L}$). The OER and HER photo/electrocatalytic polarization curves were recorded at slow scan rate (10 mVs^{-1}) to minimize the capacitive current. The detail of the electrochemical and photo electrochemical OER and HER results are demonstrated in Figs. 8 & 9.

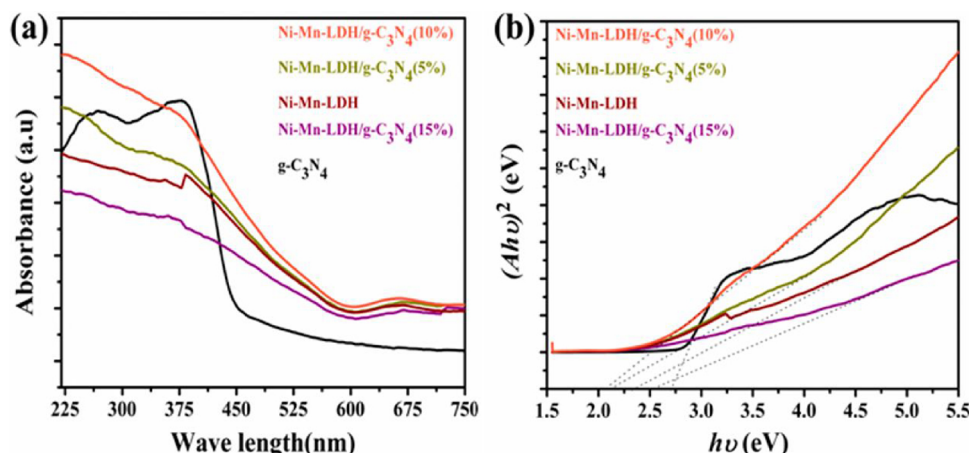


Fig. 6. (a) UV-vis./DR spectroscopic analysis (b) Plots of $(ah\nu)^2$ vs $(h\nu)$ for band gap energies of g-C₃N₄, Ni-Mn-LDH and Ni-Mn-LDH/g-C₃N₄ nanohybrids with different mass loading of g-C₃N₄.

4.1. OER photo/electrocatalytic performance

The linear sweep voltammetry (LSV) polarization curves were recorded vs RHE to investigate the OER photo/electrocatalytic performance of the as prepared Ni-Mn-LDH/g-C₃N₄ nanohybrids. For comparison similar measurements were carried out for g-C₃N₄, Ni-Mn-LDH, Ni(OH)₂/g-C₃N₄, Mn(OH)₂/g-C₃N₄ and commercial RuO₂ catalyst with same mass loading. It was observed that the electrochemical results of the Ni-Mn-LDH/g-C₃N₄ (10%) nanohybrid showed the current density of 10 mAcm⁻² by costing overpotential of 316 mV (Fig. 8a). While its photo/electrochemical results showed a profound decrease in overpotential from 316–296 mV at similar current density ($J = 10$ mAcm⁻²) under visible light illumination (Fig. 8c). The Ni-Mn-LDH/g-C₃N₄ (5%), Ni-Mn-LDH/g-C₃N₄ (15%) nanohybrids, g-C₃N₄, Ni-Mn-LDH and other reference samples such as Ni(OH)₂/g-C₃N₄ and Mn(OH)₂/g-C₃N₄ costing large overpotential for similar current density indicating weak catalytic activity (Table 2 SI). Beside this, the photo/electrocatalytic activities of the synthesized samples were further compared by recording their current densities at large onset bias (1.65 V). The corresponding results demonstrating the very sharp current density of Ni-Mn-LDH/g-C₃N₄ (10%) nanohybrid than g-C₃N₄ and Ni-Mn-LDH in the absence of light and also when illuminated under visible light with high

photo conversion efficiency (η) \approx 50.19% (Table 2). Conversely the RuO₂ afforded less onset potential while its current density at 1.65 V fell down than our Ni-Mn-LDH/g-C₃N₄ (10%) nanohybrid. Similarly among three Ni-Mn-LDH/g-C₃N₄ nanohybrids investigated here with diverse amount of g-C₃N₄, the electrochemical OER activities have order Ni-Mn-LDH/g-C₃N₄ (10%) > Ni-Mn-LDH/g-C₃N₄ (5%) > Ni-Mn-LDH/g-C₃N₄ (15%). This increase in catalytic performance from 5% to 10% and then decrease in Ni-Mn-LDH/g-C₃N₄ (15%) was due to surface saturation of Ni-Mn-LDH with g-C₃N₄ nano sheets. This could considerably effect the size and thickness of Ni-Mn-LDH layered structure by destroying the active sites on the surface, hence slowed down or hindered the transportation of photo generated charges which influence their catalytic activity [71]. The outstanding OER photo/electrocatalytic performance of Ni-Mn-LDH/g-C₃N₄ (10%) nanohybrid was also reflected by steady-state Tafel measurements. Tafel plots of potential (V) vs. log(J) were recorded with linear portion of LSV curves at low potential fitted to the Tafel equation ($\eta = b \log j + a$). Where η is overpotential, j is the current density and b is the Tafel slope are shown in Fig. 8b. It was observed that Ni-Mn-LDH/g-C₃N₄ (10%) gave the small Tafel slope (65 mVdec⁻¹) than Ni-Mn-LDH (99 mVdec⁻¹), RuO₂ (61 mVdec⁻¹) and other counterparts (Table 2). While under visible light illumination, the Tafel slope of Ni-Mn-LDH/g-C₃N₄ (10%)

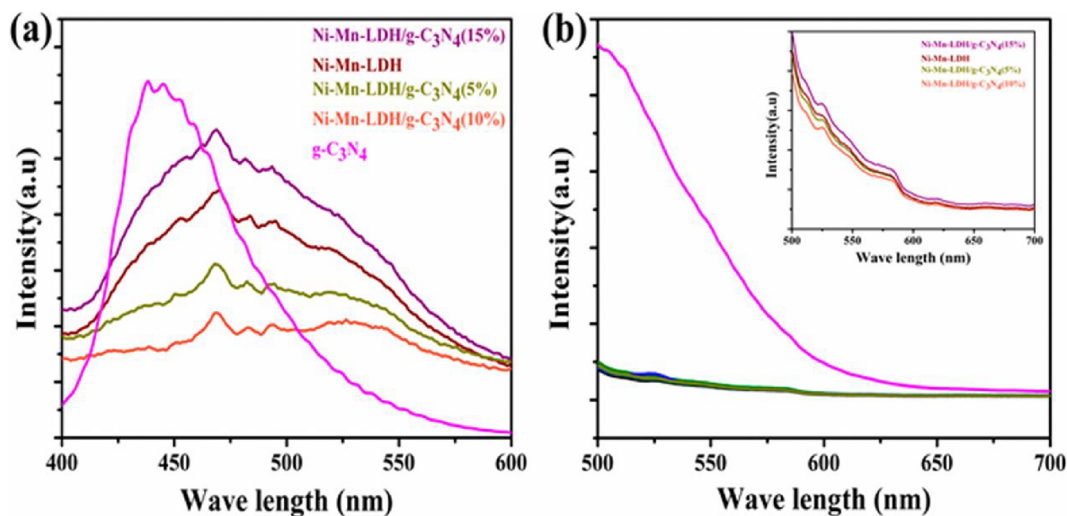


Fig. 7. (a) Photoluminescence spectra of g-C₃N₄, Ni-Mn-LDH and Ni-Mn-LDH/g-C₃N₄ nanohybrids with different percent mass of g-C₃N₄ taken at ($\lambda_{ex} = 320$ nm). (b) Photoluminescence spectra of g-C₃N₄, Ni-Mn-LDH and Ni-Mn-LDH/g-C₃N₄ nanohybrids with different percent mass of g-C₃N₄ taken at wave length higher than band gap of g-C₃N₄ ($\lambda_{ex} = 470$ nm). Inset of Fig. 7b is the partial enlarge spectra of Ni-Mn-LDH/g-C₃N₄ nanohybrids.

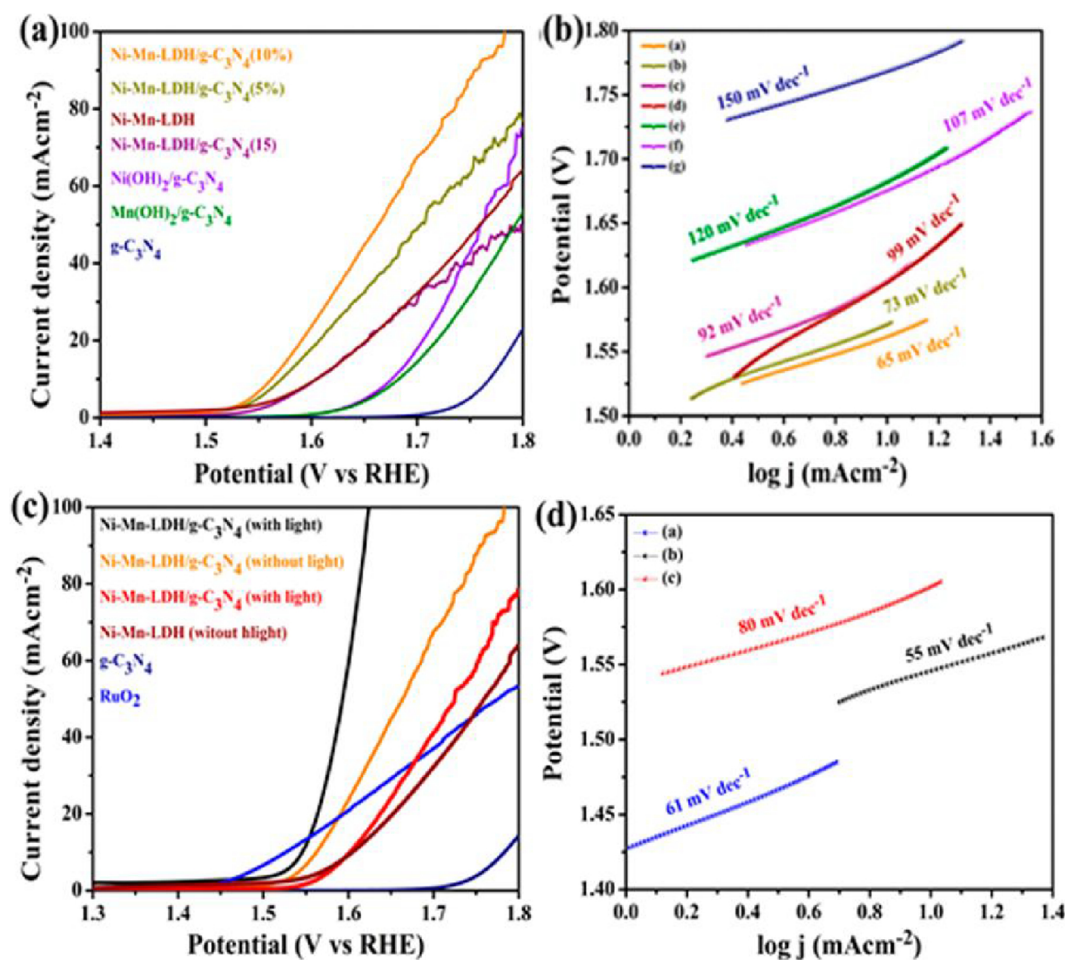


Fig. 8. Linear scan voltammogram (LSV) curves (a) LSV OER curves of Ni-Mn-LDH/g-C₃N₄ nanohybrids with different mass loading of g-C₃N₄ and other reference samples (b) “a–g” corresponding Tafel slopes (c) LSV OER curves of g-C₃N₄, Ni-Mn-LDH and Ni-Mn-LDH/g-C₃N₄ (10%) nanohybrid demonstrating the obvious effect of light on the photo/electrocatalytic activity and LSV curve of RuO₂ (d) Corresponding Tafel slopes (a) RuO₂ (b) Ni-Mn-LDH and (c) Ni-Mn-LDH/g-C₃N₄ (10%) nanohybrid.

nanohybrid was further decreased to 55 mVdec^{−1} than g-C₃N₄ and Ni-Mn-LDH (Fig. 8d). The decrease in Tafel slope could be assigned to the number of active sites on the catalyst surface correlated to rapid kinetics reveals to higher photo/electrocatalytic activity [58,72,73]. Therefore we can infer from our photo/electrochemical data that the excellent catalytic performance of Ni-Mn-LDH/g-C₃N₄ (10%) nanohybrid was mainly attributed to (i) Ni-Mn-LDH phase assigned to highly redox couple such as Ni^{2+/3+} and Mn^{3+/4+} consistent with XPS measurements (ii) The strong electrochemical association of Ni-Mn-LDH and g-C₃N₄. The g-C₃N₄ nano sheets within the nanohybrid matrix would provide conductive channel that played an irreplaceable role to create abundant active sites and assisted the charge transportation during the photo/electrochemical reactions [58]. (iii) The elastic properties of the inherent layered by layered surface morphology directly proportional to the active sites providing high ECSA for water adsorption. The layered materials afford more complementary environment for the diffusion and separation of photo excited charges [62,74,75].

4.2. HER photo/electrocatalytic performance

The photo/electrocatalytic activity of Ni-Mn-LDH/g-C₃N₄ nanohybrid was also investigated by HER water splitting. Here we just investigated the effect of light on the HER catalytic activity of the Ni-Mn-LDH/g-C₃N₄ (10%) nanohybrid. The g-C₃N₄, Ni-Mn-LDH and commercial Pt/C were used for comparison to explore the outperformance

of the Ni-Mn-LDH/g-C₃N₄ nanohybrid. The *iR*-corrected LSV measurements were recorded vs RHE are displayed in Fig. 9a. It could be seen that Ni-Mn-LDH/g-C₃N₄ nanohybrid attain current density of 60 mAcm^{−2} by costing small overpotential of −126 mV hence showing remarkable HER photo/electrocatalytic activity under visible light while without illumination it accomplish the same current density by costing high overpotential (−147 mV). In contrast the g-C₃N₄, Ni-Mn-LDH and precious metal Pt/C consume −317 mV, −162 mV and −148 mV respectively. The excellent HER photo/electrocatalytic performance of the Ni-Mn-LDH/g-C₃N₄ nanohybrid is due to the synergetic coupling of Ni-Mn-LDH and g-C₃N₄ and flexible layered structure which is more favorable for the transportation of photo excited charges. Moreover the layered structure has the capability to absorb water and ensured swelling up to some degree which maximizes the surface area that help in the photo/electrocatalysis.

The photo/electrocatalytic HER kinetics were investigated by the corresponding Tafel plots. Linear fitting of the Tafel plot of Ni-Mn-LDH/g-C₃N₄ (10%) nanohybrid with light gave a Tafel slope of 50 mVdec^{−1}, which is lower than without light (63 mVdec^{−1}), g-C₃N₄ (134 mVdec^{−1}), Ni-Mn-LDH (99 mVdec^{−1}) and Pt/C (69 mVdec^{−1}), verified the profound effect of light on the HER catalytic kinetics of Ni-Mn-LDH/g-C₃N₄ (10%) nanohybrid are shown in Fig. 9b [76–79]. It is assumed that HER kinetics and Tafel slopes followed either the Volmer-Tafel pathway (30–39 mVdec^{−1}) or the Volmer-Heyrovsky pathway (40–120 mVdec^{−1}) [80]. Both the routes included the following mechanism.

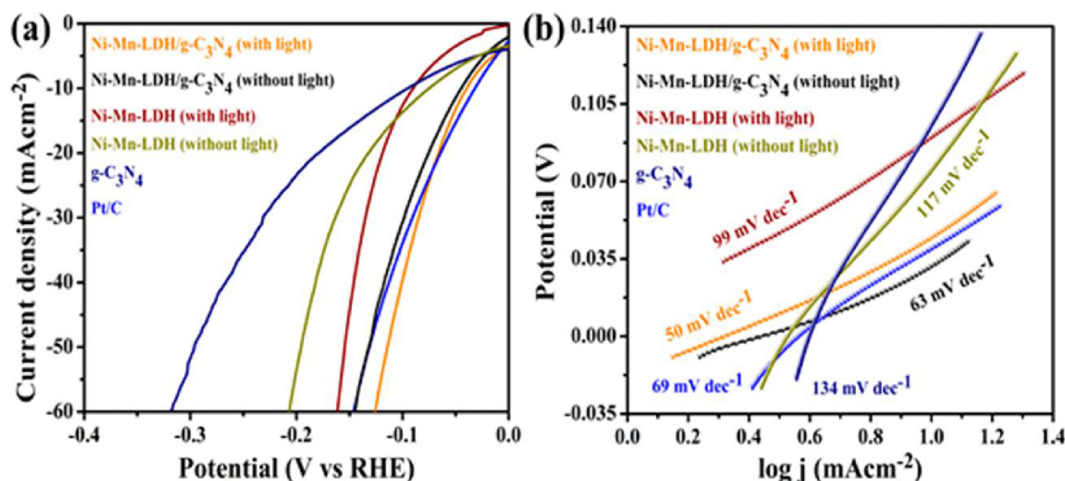
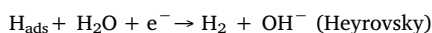
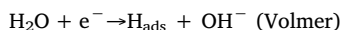
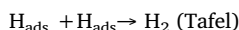
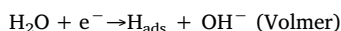


Fig. 9. (a) LSV HER curves of g-C₃N₄, Ni-Mn-LDH and Ni-Mn-LDH/g-C₃N₄ (10%) nanohybrid demonstrating the effect of visible light on the photo/electrocatalytic activity and LSV curve of Pt/C (b) corresponding Tafel slopes.



The OH⁻ are produced by the dissociation of H₂O could attach to Ni-Mn-LDH/g-C₃N₄ surface because of rigorous electrostatic attractions of the positively charged Ni^{2+/3+} and Mn^{3+/4+} species. The HER kinetics was obviously unstated based on the previous reports [73]. It was documented that when the Tafel slopes does not meet the value of 39 mVdec⁻¹, correspondingly the HER could followed a Volmer-Heyrovsky mechanism as demonstrated in our Ni-Mn-LDH/g-C₃N₄ nano hybrid [81,82]. The low Tafel slopes and more positive potential associated with rapid catalytic kinetics that might be ascribed to the promising HER photocatalytic activity of Ni-Mn-LDH/g-C₃N₄ nanohybrid (Table 3 SI). Moreover the outperformance of Ni-Mn-LDH/g-C₃N₄ nanohybrid has been investigated by comparing its OER and HER catalytic activity with literature; corresponding results provided in supporting information Table 4.

4.3. Photocatalytic degradation performance

The visible light induced photocatalytic degradation activity of Ni-

Mn-LDH/g-C₃N₄ nanohybrids and reference samples are shown in Fig. 10a. The concentration of RhB without catalyst remains unchanged by irradiating the catalytic system for 45 min indicating the stability of RhB. The photocatalytic degradation activity by the addition of catalysts have the order Ni-Mn-LDH/g-C₃N₄ (10%) > Ni-Mn-LDH/g-C₃N₄ (5%) > Ni-Mn-LDH/g-C₃N₄ (15%) > Ni-Mn-LDH > Ni(OH)₂/g-C₃N₄ > Mn(OH)₂/g-C₃N₄ > g-C₃N₄. It could be observed that g-C₃N₄ nano sheets and Ni-Mn-LDH was capable to degrade RhB up to 17% and 41% respectively under irradiations of 10 min. incredibly, the photocatalytic degradation efficiency of Ni-Mn-LDH/g-C₃N₄ nanohybrids raised up to ≥ 99% under irradiations of ≤ 10 min. The outcomes showing the Ni-Mn-LDH/g-C₃N₄ (10%) nanohybrid accounted 2.41 and 5.82 times higher photocatalytic activity than Ni-Mn-LDH and g-C₃N₄. The superior photocatalytic performance of the Ni-Mn-LDH/g-C₃N₄ nanohybrids under visible light attributed to synergistic effect of Ni-Mn-LDH and g-C₃N₄ including the energy matched band structure [67].

Conversely, profound decrease in photocatalytic activity has been seen by excessive loading of g-C₃N₄ up to (15%). The reason behind this, the high content of g-C₃N₄ considerably effect the size and thickness of Ni-Mn-LDH layered structure and diminished the active sites which hindered the transportation of photo generated charges [71,83]. Also the high contents of g-C₃N₄ weaken the bond between Ni-Mn-LDH and g-C₃N₄, hence the heterojunction could be damaged [84]. The degradation rates were measured by Eq. (−ln(C/C₀) = kt). Fig. 10b

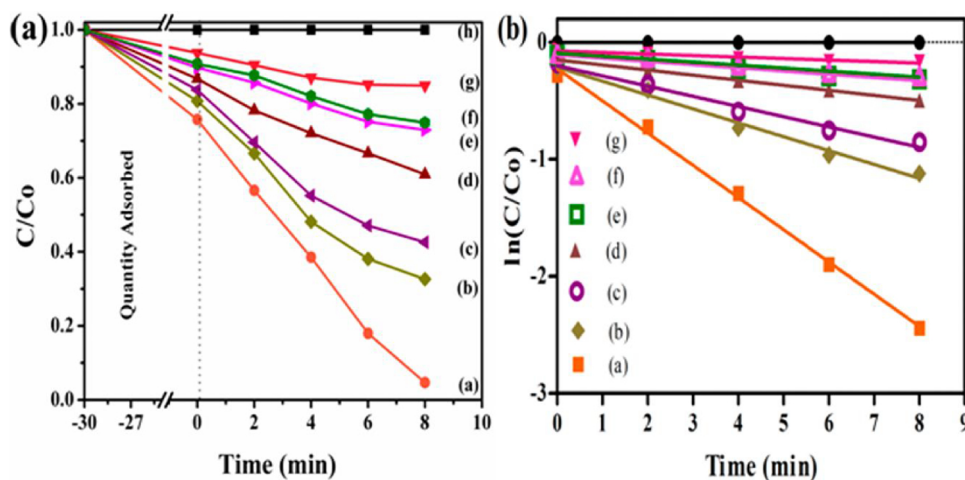
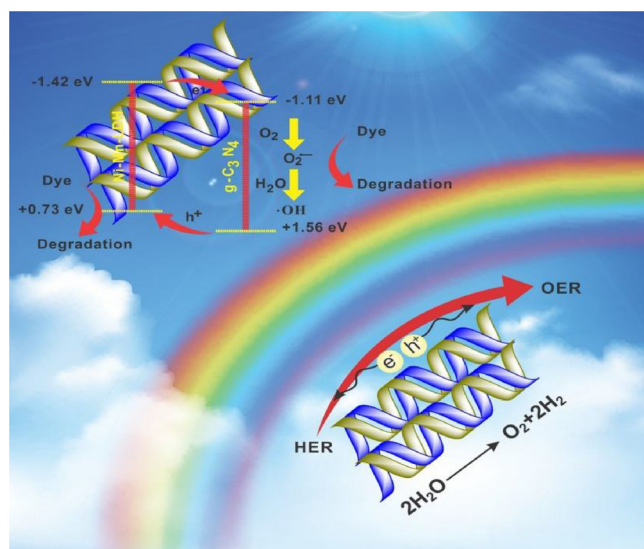


Fig. 10. (a) Photocatalytic degradation efficiency of (a–g) Ni-Mn-LDH/g-C₃N₄ (10%), Ni-Mn-LDH/g-C₃N₄ (5%), Ni-Mn-LDH/g-C₃N₄ (15%), Ni-Mn-LDH, Ni(OH)₂/g-C₃N₄, Mn(OH)₂/g-C₃N₄, g-C₃N₄ and blank (b) kinetics of degradation reaction under visible light.



Scheme 1. Graphical illustration of photo/electrocatalytic activities of the layered by layered Ni-Mn-LDH/g-C₃N₄ nanohybrid.

showed the degradation reactions followed pseudo-first-order kinetics with the rate constant (*k*) corresponding to the photocatalytic degradation activity. The rate constant of Ni-Mn-LDH/g-C₃N₄ (10%) is 7.2 and 24.2 times higher than Ni-Mn-LDH and g-C₃N₄ nano sheets under visible light assuring its superior photocatalytic activity. The corresponding photocatalytic results have been provided in supporting information Table 5.

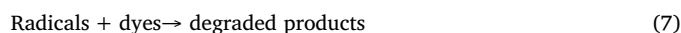
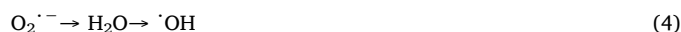
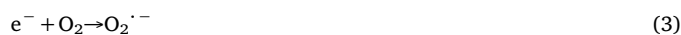
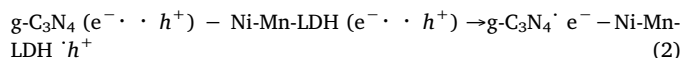
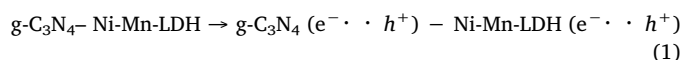
4.3.1. Photocatalytic mechanism

Advanced oxidation processes (AOPs) involve the production of very reactive oxygen species (ROSs), an efficient method to degrade the organic pollutants. During photocatalysis the photo-excitation of Ni-Mn-LDH and g-C₃N₄ surfaces generated photo excited electron-hole pairs due to suitable edge potentials. The band edge positions of the Ni-Mn-LDH and g-C₃N₄ were calculated by cyclic voltammetry under scan rate of (+3 to -3 V) to ensure the onset peaks used to calculate the CB or VB levels (Figure S₂). The conduction band (CB) of Ni-Mn-LDH was measured by Eq. $E_{CB} \text{ (eV)} = -e(4.8 - E_{FC} + E_{oxd} + E_g)$. (E_g is the CB - VB band, E_{oxd} is the onset oxidation potential, $E_{FC} = (E_{ox} + E_{red})/2 = 0.5$ is the energy level of standard ferrocene [85,86]. Similarly the CB of g-C₃N₄ was calculated by Eq. $E_{CB} \text{ (eV)} = -e(4.8 - E_{FC} + E_{red}) + E_g$. E_{red} is the onset reduction potential of g-C₃N₄ [87]. The valence band (VB) edge potentials were calculated by equation $E_g = E_{CB} - E_{VB}$. The corresponding CB and VB potentials of g-C₃N₄ was leveled at -1.11 eV and +1.56 eV, and Ni-Mn-LDH at -1.42 eV and +0.73

eV respectively [88]. The detail mechanism for the transportation of photo generated charge carriers as follows: The photo generated holes would be produced when electrons were excited from VB to CB of Ni-Mn-LDH and g-C₃N₄. As the CB edge level of g-C₃N₄ is lower than Ni-Mn-LDH, the excited electrons migrated from the Ni-Mn-LDH to the g-C₃N₄ and the holes in the VB of g-C₃N₄ migrated to Ni-Mn-LDH due to potential difference, hence taking a part in photocatalytic reactions. The overall mechanism of the transportation of photo generated charges could be seen in Scheme 1.

The major active species are the photo generated holes, $O_2^{\cdot-}$ and $\cdot OH$ taking a part in the degradation process. The formation of $O_2^{\cdot-}$ from O_2 by gaining electrons in CB and the formation of $\cdot OH$ radicals took place by $O_2^{\cdot-}$ that react with holes and H_2O to produce $\cdot OH$ radicals.

The possible photocatalytic reaction equations are:

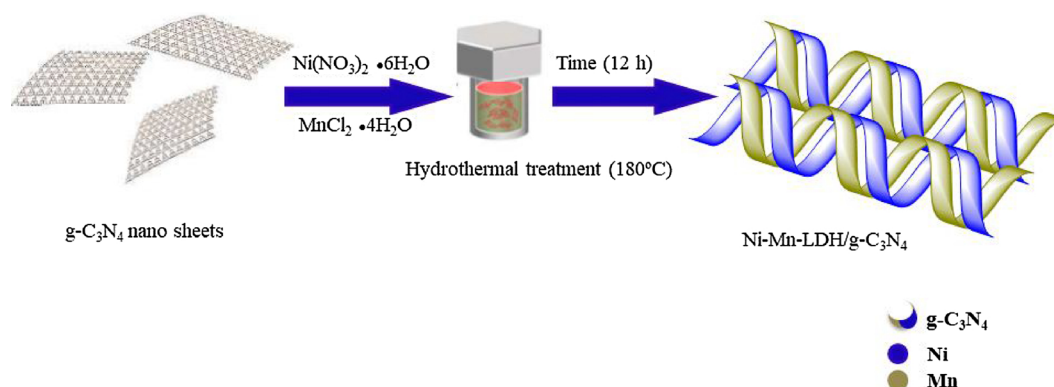


The investigations about the electronic band structure of Ni-Mn-LDH/g-C₃N₄ were examined by EPR spectra. The strong signals for hydroxyl radicals, holes and superoxide radicals were observed under visible light are shown Fig. 11a & b and in supporting information Figure S₆ respectively. A Lorentzian line centering at $g = 2.04$ indicated the generation of unpaired electrons and ascribed to the electrons trapped in O vacancies, hence verifying the successful formation of O vacancies on the surface of Ni-Mn-LDH/g-C₃N₄. Also these signals suggesting the dipolar interactions between the ions [89]. The Lorentzian line most probably due to the re-distribution of electrons within the layered heterostructure by band offsets which could help the electronic band structure for charge transportation [90].

4.4. Kinetics and the feasibility of photo/electrocatalytic reactions

A series of successive electrochemical tests were conducted to understand the mechanism of the separation and recombination of photo generated charges between g-C₃N₄ and Ni-Mn-LDH during photo/electrocatalytic reactions; detail discussions are.

The high catalytic activity of Ni-Mn-LDH/g-C₃N₄ (10%) nanohybrids could be due to the high conductivity. Therefore to test the



Scheme 2. Schematic representation of layered by layered Ni-Mn-LDH/g-C₃N₄ nanohybrid synthesized by in-situ hydrothermal treatment.

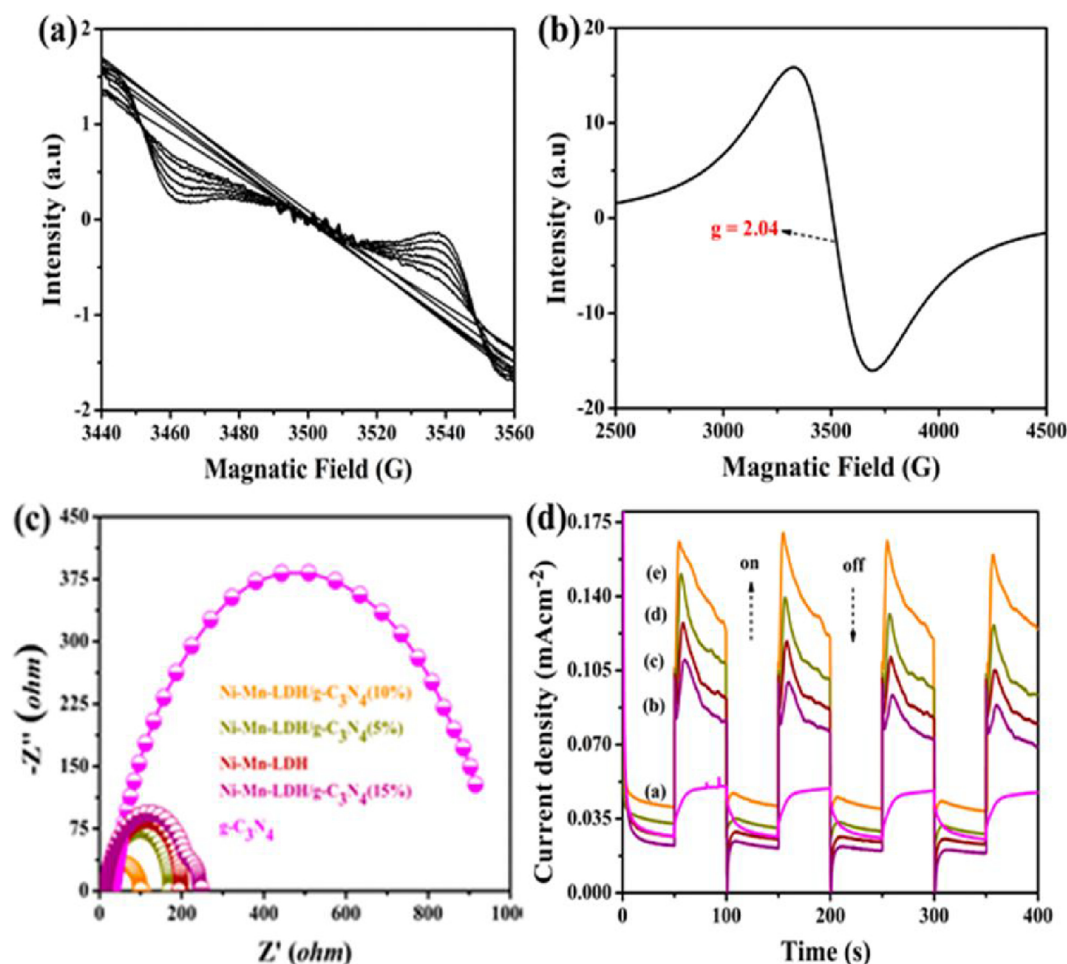


Fig. 11. (a & b) EPR spectra of Ni-Mn-LDH/g-C₃N₄ nanohybrid for hydroxyl radicals and holes respectively recorded at room temperature. (c) EIS of g-C₃N₄, Ni-Mn-LDH/g-C₃N₄ (15%), Ni-Mn-LDH and Ni-Mn-LDH/g-C₃N₄ (5%) and Ni-Mn-LDH/g-C₃N₄ (10%) nanohybrids (d) a–e Chronoamperometry curve of g-C₃N₄, Ni-Mn-LDH/g-C₃N₄ (15%), Ni-Mn-LDH, Ni-Mn-LDH/g-C₃N₄ (5%) and Ni-Mn-LDH/g-C₃N₄ (10%) nanohybrids in light and dark applying $E = +0.20$ V vs Ag/AgCl for 400 s in 1 M KOH solution.

conductivity the electrochemical impedance spectroscopy (EIS) of Ni-Mn-LDH/g-C₃N₄ (10%) nanohybrid and other counterparts were carried out. The Nyquist diagrams exhibited different obvious semicircles in the high frequency mainly correlated with (R_{ct}) are displayed in Fig. 11c. A smaller diameter semicircle Nyquist diagram can be observed in Ni-Mn-LDH/g-C₃N₄ (10%) nanohybrid than other reference samples reflected its smaller resistance with high conductivity. The EIS results demonstrated the Ni-Mn-LDH/g-C₃N₄ (10%) nanohybrid acquire smaller $R_{ct} = 96.2 \Omega$ than Ni-Mn-LDH/g-C₃N₄ (5%) $R_{ct} = 172.3 \Omega$, Ni-Mn-LDH/g-C₃N₄ (15%) $R_{ct} = 244.8 \Omega$, Ni-Mn-LDH $R_{ct} = 191.4 \Omega$ and g-C₃N₄ $R_{ct} = 920.5 \Omega$. This is responsible for its superior charge transportation capability during the photo/electrocatalytic reactions [58]. The low resistance and small Tafel slope corresponding to more favorable catalytic kinetics attributed to the synergistic coupling between the layered by layered Ni-Mn-LDH and g-C₃N₄ leading to the superior photo/electrocatalytic water splitting and photocatalytic degradation efficiency [62].

The justification about the feasible photo/electrocatalytic reactions and to understand the role of visible light, the photo-current responses of Ni-Mn-LDH/g-C₃N₄ nanohybrids, g-C₃N₄ and Ni-Mn-LDH were recorded under the chopped light. The photocurrent density of all the samples showed the on/off behavior with the pulsed light related with the recombination efficiency of photo generated charges (Fig. 11d). The photocurrent density of Ni-Mn-LDH/g-C₃N₄ (10%) nanohybrid was determined by subtracting the dark current from the total current and found as 6.60 and 1.57 times higher than g-C₃N₄ and Ni-Mn-LDH.

Moreover it could be seen that the photocurrent density of Ni-Mn-LDH/g-C₃N₄ nanohybrids increases with successive g-C₃N₄ loading up to its optimal value that reflected the significant contribution of g-C₃N₄. The results demonstrating the Ni-Mn-LDH/g-C₃N₄ nanohybrid exhibited higher photo-current responses than Ni-Mn-LDH and g-C₃N₄ leading to improve photo/electrocatalytic activity.

Electrochemically active surface area (ECSA) is directly proportional to the number of active sites considered very imperative parameter for superior photo/electrocatalytic activity. The ECSA of the g-C₃N₄, Ni-Mn-LDH and Ni-Mn-LDH/g-C₃N₄ (10%) nanohybrid were measured using (CdI) derived from CV curves at different scan rates of 10, 20, 40, 60, 80, 100 and 120 mVs⁻¹ (Figure S₁). The linear slopes of g-C₃N₄, Ni-Mn-LDH and Ni-Mn-LDH/g-C₃N₄ nanohybrid were measured as 0.168 mFcm⁻², 3.46 mFcm⁻² and 6.37 mFcm⁻² respectively (Fig. 12a). It is interesting that in the presence of g-C₃N₄, the ECSA of Ni-Mn-LDH/g-C₃N₄ nano hybrid 1.84 times higher than Ni-Mn-LDH. Such an enhanced effective surface area leading to more exposed electrocatalytic active sites and large interfacial contact area delivering the high catalytic activity [59].

The long term stability of the photo/electrocatalyst is very important parameter for effective photo/electrocatalysis. Impressively the Ni-Mn-LDH/g-C₃N₄ nanohybrid has good stability and durability when biased galvanically statically at 1.52 V for 12 h. It retain its constant current density at 10 mAcm⁻² in 1 M KOH are shown in Fig. 12b. These results exhibited the as-prepared layered by layered Ni-Mn-LDH/g-C₃N₄ nanohybrid served as best OER and HER photo/electrocatalyst with

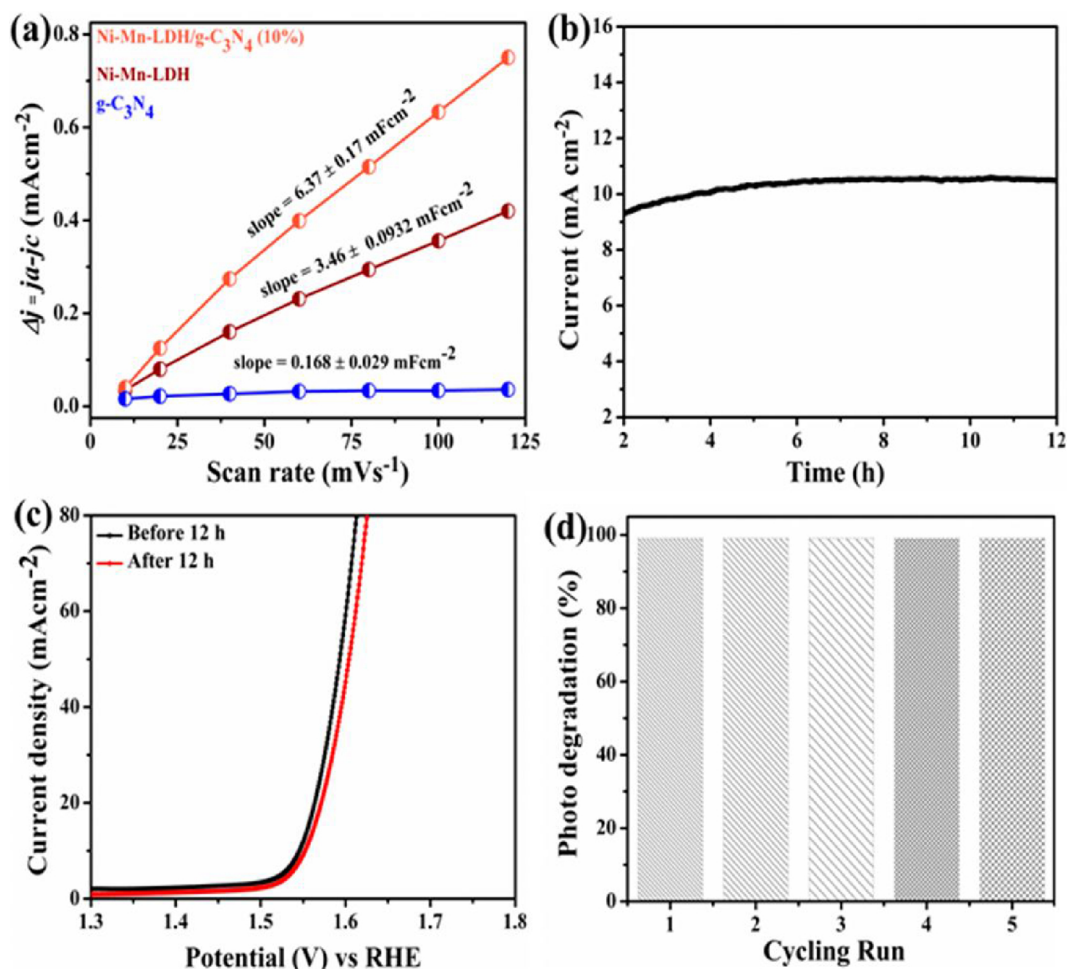


Fig. 12. (a) Charging current density ($\Delta j = j_a - j_c$) of g-C₃N₄, Ni-Mn-LDH and Ni-Mn-LDH/g-C₃N₄ (10%) plotted against scan rates. The slopes (2Cdl) were used to represent ECSA. The unit of slope is mF cm⁻² (b) Stability test of Ni-Mn-LDH/g-C₃N₄ in 1 M KOH solution (time-dependent current density curve at constant potential of 1.52 V versus Ag/AgCl) (c) LSV polarization curves of Ni-Mn-LDH/g-C₃N₄ before and after 12 h photo/electrocatalytic OER activity (d) Cycling photocatalytic degradation performance of Ni-Mn-LDH/g-C₃N₄ under visible light irradiations.

excellent activity and high stability. Furthermore the LSV polarization curve of the sample taken from the electrode after the incessant 12 h stability test was also recorded. It could be seen from Fig. 12c that Ni-Mn-LDH/g-C₃N₄ nanohybrid exhibited almost same LSV curve as initial cycle with little fade and retained its low overpotential after long time durability test. The long term stability of the Ni-Mn-LDH/g-C₃N₄ nanohybrid was also tested after the photocatalytic degradation of RhB. The Ni-Mn-LDH/g-C₃N₄ was recycled and investigated its photocatalytic activity under the same experimental condition (Fig. 12d). It keep its superior photocatalytic activity after five successive degradation cycles and can be reused for wastewater treatment. It could be noted that the morphology of the Ni-Mn-LDH/g-C₃N₄ nanohybrid was slightly agglomerated, but the structure remain substantially same after the five consecutive photocatalytic reaction (Figure S7 & S8). Therefore, we can deduce that the Ni-Mn-LDH/g-C₃N₄ nanohybrid is very stable under stirring and ultrasonic irradiations during photocatalytic reaction. Hence consider as very stable visible-light responsive material for pollution remediation.

5. Conclusion

We report a morphology controlled strategy for the fabrication of incorporated 2D layered by layered Ni-Mn-LDH/g-C₃N₄ nanohybrids with suitable electronic band structure, and demonstrated their co-enhanced photo/electrocatalytic activity for OER, HER water splitting and

photocatalytic degradation of RhB. The catalytic activities were optimized by adjusting the mass loading of g-C₃N₄ nano sheets within the nanohybrids. Significantly superior OER and HER water splitting photo/electrocatalytic activity and photocatalytic RhB degradation of Ni-Mn-LDH/g-C₃N₄ (10%) nanohybrid was attributed to the strong synergistic coupling and suitable matching of band edge potentials of Ni-Mn-LDH and g-C₃N₄. The unique conducting layered and electronic structural features shortened the distance of ions transportation and further favored the kinetics for photo/electrocatalytic reactions. These outstanding results and cost-effectiveness guaranteed a promising future material for large scale water splitting and dyes degradation.

Acknowledgement

The authors are thankful to the National Natural Science Foundation of China (grant No. 21271017), the National Science and Technology Supporting Plan of the Twelfth Five-year (No. 2014BAE12B0101) and the Fundamental Research Funds for the Central Universities (No. YS1406).

References

- [1] C. Wang, R.B. Moghaddam, M.J. Brett, S.H. Bergens, Simple aqueous preparation of high activity and stability NiFe hydrous oxide catalysts for water oxidation, *ACS Sustain. Chem. Eng.* 5 (2016) 1106–1112.
- [2] A.I. Khan, D. O'Hare, Intercalation chemistry of layered double hydroxides: recent

- developments and applications, *J. Mater. Chem.* 12 (2002) 3191–3198.
- [3] Y. Liang, Y. Li, H. Wang, H. Dai, Strongly coupled inorganic/nanocarbon hybrid materials for advanced electrocatalysis, *J. Am. Chem. Soc.* 135 (2013) 2013–2036.
 - [4] M. Gong, Y. Li, H. Wang, Y. Liang, J.Z. Wu, J. Zhou, J. Wang, T. Regier, F. Wei, H. Dai, An advanced Ni-Fe layered double hydroxide electrocatalyst for water oxidation, *J. Am. Chem. Soc.* 135 (2013) 8452–8455.
 - [5] R. Marschall, Semiconductor composites: strategies for enhancing charge carrier separation to improve photocatalytic activity, *Adv. Funct. Mater.* 24 (2014) 2421–2440.
 - [6] W. Choi, A. Termin, M.R. Hoffmann, The role of metal ion dopants in quantum-sized TiO₂: correlation between photo reactivity and charge carrier recombination dynamics, *J. Phys. Chem.* 98 (1994) 13669–13679.
 - [7] J.Z. Bloh, R. Dillert, D.W. Bahnemann, Designing optimal metal-doped photocatalysts: correlation between photocatalytic activity, doping ratio, and particle size, *J. Phys. Chem. C* 116 (2012) 25558–25562.
 - [8] F. Wang, C. Di Valentin, G. Pacchioni, Rational band gap engineering of WO₃ photocatalyst for visible light water splitting, *ChemCatChem* 4 (2012) 476–478.
 - [9] W. Liu, Y. Shang, A. Zhu, P. Tan, Y. Liu, L. Qiao, D. Chu, X. Xiong, J. Pan, Enhanced performance of doped BiOCl nanoplates for photocatalysis: understanding from doping insight into improved spatial carrier separation, *J. Mater. Chem. A* 5 (2017) 12542–12549.
 - [10] R. Asahi, T. Morikawa, T. Ohwaki, K. Aoki, Y. Taga, Visible-light photocatalysis in nitrogen-doped titanium oxides, *Science* 293 (2001) 269–271.
 - [11] S. Linic, P. Christopher, D.B. Ingram, Plasmonic-metal nanostructures for efficient conversion of solar to chemical energy, *Nat. Mater.* 10 (2011) 911.
 - [12] W. Hou, S.B. Cronin, A review of surface plasmon resonance-enhanced photocatalysis, *Adv. Funct. Mater.* 23 (2013) 1612–1619.
 - [13] J. Das, B. Patra, N. Baliarsingh, K. Parida, Adsorption of phosphate by layered double hydroxides in aqueous solutions, *Appl. Clay Sci.* 32 (2006) 252–260.
 - [14] S. Singha, M. Sahoo, K. Parida, Highly active Pd nanoparticles dispersed on amine functionalized layered double hydroxide for Suzuki coupling reaction, *Dalton Trans.* 40 (2011) 7130–7132.
 - [15] L. Mohapatra, K. Parida, A review on the recent progress, challenges and perspective of layered double hydroxides as promising photocatalysts, *J. Mater. Chem. A* 4 (2016) 10744–10766.
 - [16] R. Subbaraman, D. Tripkovic, K.-C. Chang, D. Strmcnik, A.P. Paulikas, P. Hirunsit, M. Chan, J. Greeley, V. Stamenkovic, N.M. Markovic, Trends in activity for the water electrolyser reactions on 3d M (Ni, Co, Fe, Mn) hydr (oxy) oxide catalysts, *Nat. Mater.* 11 (2012) 550.
 - [17] X. Li, F.C. Walsh, D. Pletcher, Nickel based electrocatalysts for oxygen evolution in high current density, alkaline water electrolyzers, *Phys. Chem. Chem. Phys.* 13 (2011) 1162–1167.
 - [18] L. Trotochaud, J.K. Ranney, K.N. Williams, S.W. Boettcher, Solution-cast metal oxide thin film electrocatalysts for oxygen evolution, *J. Am. Chem. Soc.* 134 (2012) 17253–17261.
 - [19] A.J. Esswein, M.J. McMurdo, P.N. Ross, A.T. Bell, T.D. Tilley, Size-dependent activity of Co₃O₄ nanoparticle anodes for alkaline water electrolysis, *J. Phys. Chem. C* 113 (2009) 15068–15072.
 - [20] U. Lačnjevac, B. Jović, J. Jović, N. Krstajić, Determination of kinetic parameters for the hydrogen evolution reaction on the electrodeposited Ni–MoO₂ composite coating in alkaline solution, *J. Electroanal. Chem.* 677 (2012) 31–40.
 - [21] M. Sarno, A. Garamella, C. Cirillo, P. Ciambelli, MoS₂/MoO₃/graphene electrocatalyst for HER, *Chem. Eng. Trans.* submitted (2014).
 - [22] F. Su, S.C. Mathew, L. Möhlmann, M. Antonietti, X. Wang, S. Blechert, Aerobic oxidative coupling of amines by carbon nitride photocatalysis with visible light, *Angew. Chem. Int. Ed.* 50 (2011) 657–660.
 - [23] A.B. Jorge, D.J. Martin, M.T. Dhanoo, A.S. Rahman, N. Makwana, J. Tang, A. Sella, F. Corà, S. Firth, J.A. Darr, H₂ and O₂ evolution from water half-splitting reactions by graphitic carbon nitride materials, *J. Phys. Chem. C* 117 (2013) 7178–7185.
 - [24] S. Zhang, J. Li, M. Zeng, G. Zhao, J. Xu, W. Hu, X. Wang, In situ synthesis of water-soluble magnetic graphitic carbon nitride photocatalyst and its synergistic catalytic performance, *ACS Appl. Mater. Interfaces* 5 (2013) 12735–12743.
 - [25] M. Xiong, L. Chen, Q. Yuan, J. He, S.-L. Luo, C.-T. Au, S.-F. Yin, Controlled synthesis of graphitic carbon nitride/beta bismuth oxide composite and its high visible-light photocatalytic activity, *Carbon* 86 (2015) 217–224.
 - [26] J. He, L. Chen, Z.-Q. Yi, D. Ding, C.-T. Au, S.-F. Yin, Fabrication of two-dimensional porous CdS nanoplates decorated with C₃N₄ nanosheets for highly efficient photocatalytic hydrogen production from water splitting, *Catal. Commun.* 99 (2017) 79–82.
 - [27] Y. Zheng, Y. Jiao, Y. Zhu, L.H. Li, Y. Han, Y. Chen, A. Du, M. Jaroniec, S.Z. Qiao, Hydrogen evolution by a metal-free electrocatalyst, *Nat. Commun.* 5 (2014) 3783.
 - [28] Y. Cheng, S.P. Jiang, Advances in electrocatalysts for oxygen evolution reaction of water electrolysis-from metal oxides to carbon nano tubes, *Prog. Nat. Sci. Mater.* 25 (2015) 545–553.
 - [29] F. Su, S.C. Mathew, G. Lipner, X. Fu, M. Antonietti, S. Blechert, X. Wang, mpg-C₃N₄-catalyzed selective oxidation of alcohols using O₂ and visible light, *J. Am. Chem. Soc.* 132 (2010) 16299–16301.
 - [30] X. Lu, Q. Wang, D. Cui, Preparation and photocatalytic properties of g-C₃N₄/TiO₂ hybrid composite, *J. Mater. Sci. Technol.* 26 (2010) 925–930.
 - [31] X. Wang, K. Maeda, A. Thomas, K. Takanabe, G. Xin, J.M. Carlsson, K. Domen, M. Antonietti, A metal-free polymeric photocatalyst for hydrogen production from water under visible light, *Nat. Mater.* 8 (2009) 76.
 - [32] Y. Zhang, M. Antonietti, Photocurrent generation by polymeric carbon nitride solids: an initial step towards a novel photovoltaic system, *Chem. Asian J.* 5 (2010) 1307–1311.
 - [33] P. Wardman, Reduction potentials of one-electron couples involving free radicals in aqueous solution, *J. Phys. Chem. Ref. Data* 18 (1989) 1637–1755.
 - [34] H. Park, W. Choi, M.R. Hoffmann, Effects of the preparation method of the ternary CdS/TiO₂/Pt hybrid photocatalysts on visible light-induced hydrogen production, *J. Mater. Chem.* 18 (2008) 2379–2385.
 - [35] M.D. Symes, L. Cronin, Decoupling hydrogen and oxygen evolution during electrolytic water splitting using an electron-coupled-proton buffer, *Nat. Chem.* 5 (2013) 403.
 - [36] N. Baliarsingh, K. Parida, G. Pradhan, Influence of the nature and concentration of precursor metal ions in the brucite layer of LDHs for phosphate adsorption—a review, *RSC Adv.* 3 (2013) 23865–23878.
 - [37] M. Shakeel, B. Li, M. Arif, G. Yasin, W. Rehman, A.U. Khan, S. Khan, A. Khan, J. Ali, Controlled synthesis of highly proficient and durable hollow hierarchical heterostructured (Ag-AgBr)/HHST: a UV and visible light active photocatalyst in degradation of organic pollutants, *Appl. Catal. B: Environ.* 227 (2018) 433–445.
 - [38] M. Arif, G. Yasin, M. Shakeel, X. Fang, R. Gao, S. Ji, D. Yan, Coupling of bifunctional CoMn-layered double Hydroxide@GraphiticC₃N₄ nanohybrids towards efficient photoelectrochemical overall Water splitting, *Chem. Asian J.* 13 (2018) 1045–1052.
 - [39] M. Shakeel, B. Li, G. Yasin, M. Arif, W. Rehman, H.D. Khan, In situ fabrication of foamed titania carbon nitride nanocomposite and its synergetic visible light photocatalytic performance, *Ind. Eng. Chem. Res.* 57 (2018) 8152–8159.
 - [40] Y. Wang, X. Wang, M. Antonietti, Polymeric graphitic carbon nitride as a heterogeneous organocatalyst: from photochemistry to multipurpose catalysis to sustainable chemistry, *Angew. Chem. Int. Ed.* 51 (2012) 68–89.
 - [41] J. Zhang, M. Zhang, L. Lin, X. Wang, Sol processing of conjugated carbon nitride powders for thin-film fabrication, *Angew. Chem.* 127 (2015) 6395–6399.
 - [42] P. Tan, X. Chen, L. Wu, Y.Y. Shang, W. Liu, J. Pan, X. Xiong, Hierarchical flower-like SnSe₂ supported Ag₃PO₄ nanoparticles: towards visible light driven photocatalyst with enhanced performance, *Appl. Catal. B: Environ.* 202 (2017) 326–334.
 - [43] J. Liu, T. Zhang, Z. Wang, G. Dawson, W. Chen, Simple pyrolysis of urea into graphitic carbon nitride with recyclable adsorption and photocatalytic activity, *J. Mater. Chem.* 21 (2011) 14398–14401.
 - [44] J.-X. Sun, Y.-P. Yuan, L.-G. Qiu, X. Jiang, A.-J. Xie, Y.-H. Shen, J.-F. Zhu, Fabrication of composite photocatalyst gC₃N₄-ZnO and enhancement of photocatalytic activity under visible light, *Dalton Trans.* 41 (2012) 6756–6763.
 - [45] F. Millange, R.I. Walton, D. O'Hare, Time-resolved in situ X-ray diffraction study of the liquid-phase reconstruction of Mg–Al–carbonate hydroxalcalite-like compounds, *J. Mater. Chem.* 10 (2000) 1713–1720.
 - [46] S. Nayak, L. Mohapatra, K. Parida, Visible light-driven novel gC₃N₄/NiFe-LDH composite photocatalyst with enhanced photocatalytic activity towards water oxidation and reduction reaction, *J. Mater. Chem. A* 3 (2015) 18622–18635.
 - [47] L. Zhang, L. Li, X. Sun, P. Liu, D. Yang, X. Zhao, ZnO-layered double Hydroxide@graphitic carbon nitride composite for consecutive adsorption and photodegradation of dyes under UV and visible lights, *Materials* 9 (2016) 927.
 - [48] S.J. Kim, Y. Lee, D.K. Lee, J.W. Lee, J.K. Kang, Efficient Co-Fe layered double hydroxide photocatalysts for water oxidation under visible light, *J. Mater. Chem. A* 2 (2014) 4136–4139.
 - [49] J. Yu, S. Wang, B. Cheng, Z. Lin, F. Huang, Noble metal-free Ni (OH)₂-gC₃N₄ composite photocatalyst with enhanced visible-light photocatalytic H₂-production activity, *J. Adv. Catal. Sci.* 3 (2013) 1782–1789.
 - [50] M. Gao, W. Sheng, Z. Zhuang, Q. Fang, S. Gu, J. Jiang, Y. Yan, Efficient water oxidation using nanostructured α-nickel-hydroxide as an electrocatalyst, *J. Am. Chem. Soc.* 136 (2014) 7077–7084.
 - [51] Q. Tang, L. Jiang, J. Liu, S. Wang, G. Sun, Effect of surface manganese valence of manganese oxides on the activity of the oxygen reduction reaction in alkaline media, *ACS Catal.* 4 (2014) 457–463.
 - [52] L. Xu, Y.-S. Ding, C.-H. Chen, L. Zhao, C. Rimkus, R. Joesten, S.L. Suib, 3D flower-like α-nickel hydroxide with enhanced electrochemical activity synthesized by microwave-assisted hydrothermal method, *Chem. Mater.* 20 (2007) 308–316.
 - [53] P. Jeevanandam, Y. Koltypin, A. Gedanken, Synthesis of nanosized α-nickel hydroxide by a sonochemical method, *Nano Lett.* 1 (2001) 263–266.
 - [54] H.-T. Tung, J.-M. Song, S.-W. Feng, C. Kuo, I.-G. Chen, Dependence of surface atomic arrangement of titanium dioxide on metallic nanowire nucleation by thermally assisted photoreduction, *Phys. Chem. Chem. Phys.* 12 (2010) 740–744.
 - [55] L. Spanhel, M. Haase, H. Weller, A. Henglein, Photochemistry of colloidal semiconductors. 20. Surface modification and stability of strong luminescing CdS particles, *J. Am. Chem. Soc.* 109 (1987) 5649–5655.
 - [56] Y. He, J. Cai, T. Li, Y. Wu, Y. Yi, M. Luo, L. Zhao, Synthesis, characterization, and activity evaluation of DyVO₄/g-C₃N₄ composites under visible-light irradiation, *Ind. Eng. Chem. Res.* 51 (2012) 14729–14737.
 - [57] Y. Ma, Y. Bian, Y. Liu, A. Zhu, H. Wu, H. Cui, D. Chu, J. Pan, Construction of Z-Scheme system for enhanced photocatalytic H₂ evolution based on CdS quantum Dots/CeO₂ nanorods heterojunction, *ACS Sustain. Chem. Eng.* 6 (2018) 2552–2562.
 - [58] X. Han, C. Yu, J. Yang, C. Zhao, H. Huang, Z. Liu, P.M. Ajayan, J. Qiu, Mass and charge transfer coenhanced oxygen evolution behaviors in CoFe-layered double hydroxide assembled on graphene, *Adv. Mater. Interfaces* 3 (2016).
 - [59] K. Fan, H. Chen, Y. Ji, H. Huang, P.M. Claesson, Q. Daniel, H. Rensmo, F. Li, Y. Luo, Nickel–vanadium monolayer double hydroxide for efficient electrochemical water oxidation, *Nat. Commun.* 7 (2016) 11981.
 - [60] M. Chakraborty, S. Dasgupta, C. Soundrapandian, J. Chakraborty, S. Ghosh, M.K. Mitra, D. Basu, Methotrexate intercalated Zn-Al-layered double hydroxide, *J. Solid State Chem.* 184 (2011) 2439–2445.
 - [61] M.C. Biesinger, B.P. Payne, A.P. Grosvenor, L.W. Lau, A.R. Gerson, R.S.C. Smart, Resolving surface chemical states in XPS analysis of first row transition metals, oxides and hydroxides: Cr, Mn, Fe, Co and Ni, *Appl. Surf. Sci.* 257 (2011) 2717–2730.
 - [62] J. Wu, Z. Ren, S. Du, L. Kong, B. Liu, W. Xi, J. Zhu, H. Fu, A highly active oxygen

- evolution electrocatalyst: ultrathin CoNi double hydroxide/CoO nanosheets synthesized via interface-directed assembly, *Nano Res.* 9 (2016) 713–725.
- [63] Z. Xu, H. Zeng, Decomposition pathways of hydrotalcite-like compounds $\text{Mg}_{1-x}\text{Al}_x(\text{OH})_2(\text{NO}_3)_x \cdot n\text{H}_2\text{O}$ as a continuous function of nitrate anions, *Chem. Mater.* 13 (2001) 4564–4572.
- [64] P. Kuśtrowski, D. Sułkowska, L. Chmielarz, A. Rafalska-Lasocha, B. Dudek, R. Dziembaj, Influence of thermal treatment conditions on the activity of hydrotalcite-derived Mg–Al oxides in the aldol condensation of acetone, *Microporous Mesoporous Mater.* 78 (2005) 11–22.
- [65] M.Q. Zhao, Q. Zhang, J.Q. Huang, F. Wei, Hierarchical nanocomposites derived from nanocarbons and layered double hydroxides-properties, synthesis, and applications, *Adv. Funct. Mater.* 22 (2012) 675–694.
- [66] K.-i. Katsumata, R. Motoyoshi, N. Matsushita, K. Okada, Preparation of graphitic carbon nitride (gC_3N_4)/ WO_3 composites and enhanced visible-light-driven photo-degradation of acetaldehyde gas, *J. Hazard. Mater.* 260 (2013) 475–482.
- [67] Y. Shang, X. Chen, W. Liu, P. Tan, H. Chen, L. Wu, C. Ma, X. Xiong, J. Pan, Photocorrosion inhibition and high-efficiency photoactivity of porous $\text{gC}_3\text{N}_4/\text{Ag}_2\text{CrO}_4$ composites by simple microemulsion-assisted co-precipitation method, *Appl. Catal. B: Environ.* 204 (2017) 78–88.
- [68] W. Zeng, Y. Bian, S. Cao, Y. Ma, Y. Liu, A. Zhu, P. Tan, J. Pan, Phase transformation synthesis of strontium tantalum oxynitride-based heterojunction for improved visible light-driven hydrogen evolution, *ACS Appl. Mater. Interfaces* 10 (2018) 21328–21334.
- [69] X. Jia, Y. Zhao, G. Chen, L. Shang, R. Shi, X. Kang, G.I. Waterhouse, L.Z. Wu, C.H. Tung, T. Zhang, Ni_3FeN nanoparticles derived from ultrathin NiFe -Layered double hydroxide nanosheets: an efficient overall Water splitting electrocatalyst, *Adv. Energy Mater.* 6 (2016) 10.
- [70] V.N. Khabashesku, J.L. Zimmerman, J.L. Margrave, Powder synthesis and characterization of amorphous carbon nitride, *Chem. Mater.* 12 (2000) 3264–3270.
- [71] M. Murdoch, G. Waterhouse, M. Nadeem, J. Metson, M. Keane, R. Howe, J. Llorca, H. Idriss, The effect of gold loading and particle size on photocatalytic hydrogen production from ethanol over Au/TiO_2 nanoparticles, *Nat. Chem.* 3 (2011) 489.
- [72] M. Tahir, N. Mahmood, L. Pan, Z.-F. Huang, Z. Lv, J. Zhang, F.K. Butt, G. Shen, X. Zhang, S.X. Dou, Efficient water oxidation through strongly coupled graphitic C_3N_4 coated cobalt hydroxide nanowires, *J. Mater. Chem. A* 4 (2016) 12940–12946.
- [73] Z. Liu, C. Yu, X. Han, J. Yang, C. Zhao, H. Huang, J. Qiu, CoMn layered double Hydroxides/Carbon nanotubes architectures as high-performance electrocatalysts for the oxygen evolution reaction, *ChemElectroChem* 3 (2016) 906–912.
- [74] X. Lin, T. Huang, F. Huang, W. Wang, J. Shi, Photocatalytic activity of a Bi-based oxychloride $\text{Bi}_3\text{O}_4\text{Cl}$, *J. Phys. Chem. B* 110 (2006) 24629–24634.
- [75] A. Mantilla, G. Jácome-Acatitla, G. Morales-Mendoza, F. Tzompantzi, R. Gómez, Photoassisted degradation of 4-chlorophenol and p-cresol using MgAl hydrotalcites, *Ind. Eng. Chem. Res.* 50 (2010) 2762–2767.
- [76] B. You, N. Jiang, M. Sheng, S. Gul, J. Yano, Y. Sun, High-performance overall water splitting electrocatalysts derived from cobalt-based metal–organic frameworks, *Chem. Mater.* 27 (2015) 7636–7642.
- [77] P.F. Liu, S. Yang, B. Zhang, H.G. Yang, Defect-rich ultrathin Cobalt–Iron layered double hydroxide for electrochemical overall Water splitting, *ACS Appl. Mater. Interfaces* 8 (2016) 34474–34481.
- [78] Y. Tang, X. Fang, X. Zhang, G. Fernandes, Y. Yan, D. Yan, X. Xiang, J. He, Space-confined earth-abundant bifunctional electrocatalyst for High-efficiency Water splitting, *ACS Appl. Mater. Interfaces* 9 (2017) 36762–36771.
- [79] B. Bayatsarmadi, Y. Zheng, V. Russo, L. Ge, C.S. Casari, S.-Z. Qiao, Highly active nickel–cobalt/nanocarbon thin films as efficient water splitting electrodes, *Nanoscale* 8 (2016) 18507–18515.
- [80] M. Gong, W. Zhou, M.-C. Tsai, J. Zhou, M. Guan, M.-C. Lin, B. Zhang, Y. Hu, D.-Y. Wang, J. Yang, Nanoscale nickel oxide/nickel heterostructures for active hydrogen evolution electrocatalysis, *Nat. Commun.* 5 (2014) 4695.
- [81] M.P.M. Kaninski, V.M. Nikolic, G.S. Tasic, Z.L. Rakocovic, Electrocatalytic activation of Ni electrode for hydrogen production by electrodeposition of Co and V species, *Int. J. Hydrogen Energy* 34 (2009) 703–709.
- [82] J. Yin, P. Zhou, L. An, L. Huang, C. Shao, J. Wang, H. Liu, P. Xi, Self-supported nanoporous NiCo_2O_4 nanowires with cobalt–nickel layered oxide nanosheets for overall water splitting, *Nanoscale* 8 (2016) 1390–1400.
- [83] D. Jassby, J. Farner Budarz, M. Wiesner, Impact of aggregate size and structure on the photocatalytic properties of TiO_2 and ZnO nanoparticles, *Environ. Sci. Technol.* 46 (2012) 6934–6941.
- [84] J. Lu, I. Do, L.T. Drzal, R.M. Worden, I. Lee, Nanometal-decorated exfoliated graphite nanoplatelet based glucose biosensors with high sensitivity and fast response, *ACS Nano* 2 (2008) 1825–1832.
- [85] F.K. Shehzad, Y. Zhou, L. Zhang, Y. Long, I. Maitlo, A. Iqbal, D. Yang, Anionic effect of δ and γ forms of tris (alkoxo) ligand functionalized anderson-type polyoxometalates on nonlinear optical response of Porphyrin–POM based supramolecular compounds, *J. Phys. Chem. C* 122 (2018) 1280–1287.
- [86] H.M. Asif, Y. Zhou, L. Zhang, N. Shaheen, D. Yang, J. Li, Y. Long, A. Iqbal, Y. Li, Covalent synthesis of Two hybrids composed of dawson-type polyoxometalate and porphyrin with remarkable Third-order optical nonlinearities reflecting the effect of polyoxometalates, *Inorg. Chem.* 56 (2017) 9436–9447.
- [87] X. Sun, Y. Liu, S. Chen, W. Qiu, G. Yu, Y. Ma, T. Qi, H. Zhang, X. Xu, D. Zhu, X-Shaped electroactive molecular materials based on oligothiophene architectures: facile synthesis and photophysical and electrochemical properties, *Adv. Funct. Mater.* 16 (2006) 917–925.
- [88] J. Cui, Y. Li, L. Liu, L. Chen, J. Xu, J. Ma, G. Fang, E. Zhu, H. Wu, L. Zhao, Near-infrared plasmonic-enhanced solar energy harvest for highly efficient photocatalytic reactions, *Nano Lett.* 15 (2015) 6295–6301.
- [89] K. Li, S. Gao, Q. Wang, H. Xu, Z. Wang, B. Huang, Y. Dai, J. Lu, In-situ-reduced synthesis of Ti^{3+} self-doped $\text{TiO}_2/\text{g-C}_3\text{N}_4$ heterojunctions with high photocatalytic performance under LED light irradiation, *ACS Appl. Mater. Interfaces* 7 (2015) 9023–9030.
- [90] J. Zhang, M. Zhang, R.Q. Sun, X. Wang, A facile band alignment of polymeric carbon nitride semiconductors to construct isotype heterojunctions, *Angew. Chem.* 124 (2012) 10292–10296.